6224 *Biochemistry* **2009,** *48,* 6224–6239
DOI: 10.1021/bi802266g

BIOCHEMISTRY
including biophysical chemistry & molecular biology
Article

Kinetic, Dynamic, Ligand Binding Properties, and Structural Models of a Dual-Substrate Specific Nudix Hydrolase from *Schizosaccharomyces pombe*[†,‡]

John A. Garza, Udayar Ilangovan, Andrew P. Hinck, and Larry D. Barnes*

Department of Biochemistry, The University of Texas Health Science Center at San Antonio, 7703 Floyd Curl Drive, San Antonio, Texas 78229-3900

Received December 11, 2008; Revised Manuscript Received April 1, 2009

ABSTRACT: *Schizosaccharomyces pombe* Aps1 is a nudix hydrolase that catalyzes the hydrolysis of both diadenosine 5′,5‴-P^1,P^n-oligophosphates and diphosphoinositol polyphosphates *in vitro*. Nudix hydrolases act upon a wide variety of substrates, despite having a common 23 amino acid catalytic motif; hence, the residues responsible for substrate specificity are considered to reside outside the common catalytic nudix motif. The specific residues involved in binding each substrate of *S. pombe* Aps1 are unknown. In this study, we have conducted mutational and kinetic studies in combination with structural homology modeling and NMR spectroscopic analyses to identify potential residues involved in binding each class of substrates. This study demonstrates several major findings with regard to Aps1. First, the determination of the kinetic parameters of K_m and k_{cat} indicated that the initial 31 residues of Aps1 are not involved in substrate binding or catalysis with respect to Ap_6A. Second, NMR spectroscopic analyses revealed the secondary structure and three dynamic backbone regions, one of which corresponds to a large insert in Aps1 as compared to other putative fungal orthologues. Third, two structural models of Aps1Δ2−19, based on the crystal structures of human DIPP1 and *T. thermophilus* Ndx1, were generated using homology modeling. The structural models were in excellent agreement with the NMR-derived secondary structure of Aps1Δ2−19. Fourth, NMR chemical shift mapping in conjunction with structural homology models indicated several residues outside the catalytic nudix motif that are involved in specific binding of diphosphoinositol polyphosphate or diadenosine oligophosphate ligands.

Schizosaccharomyces pombe Aps1[1] is a member of the nudix motif protein family, which is composed of over 8000 putative members (*1*). The nudix nomenclature was proposed on the basis of the observation that nudix hydrolases generally hydrolyze a nucleoside diphosphate linked to some moiety X (*2*). The numerous such substrates have been recently reviewed (*3*). Nudix hydrolases are characterized by the 23 amino acid sequence motif $GX_5EX_7REUXEEXGU$, where X is any amino acid, and U is a bulky hydrophobic amino acid I, L, or V (*2*). It has been proposed that nudix hydrolases degrade potentially deleterious nucleoside derivatives and regulate levels of metabolic intermediates (*2*, *4*). Recent observations that nudix hydrolases participate in such diverse processes as decapping of mRNA (*5*−*7*), activation of a bacterial alcohol dehydrogenase (*8*), and gating of a calcium-permeable channel (*9*) indicate that nudix hydrolases have broader functions, as noted by McLennan (*3*). In addition, nudix hydrolases are now known to act upon a variety of non-nucleotide substrates, e.g., diphosphoinositol polyphosphates (*4*, *10*, *11*), in addition to nucleoside diphosphate derivatives.

Aps1 is composed of 210 amino acids and behaves as a monomer in solution (*12*). It catalyzes the hydrolysis of both diadenosine 5′,5‴-P′,P^n-oligophosphates, Ap_nA (n = 4−6), with Ap_6A and Ap_5A being preferred over Ap_4A *in vitro*, and diphosphoinositol polyphosphates, diphosphoinositol pentakisphosphate (IP_7), and bisdiphosphoinositol tetrakisphosphate (IP_8) *in vitro* (*4*). It is likely that these two classes of substrates compete with each other kinetically since there is a common set of catalytic residues in the Nudix motif (*4*, *13*, *14*). Studies by Safrany et al.

[†]This work was supported by the National Institutes of Health (GM58670 to A.H.) and the Robert A. Welch Foundation (AQ1431 to A.H.). Structural studies made use of the San Antonio Cancer Institute Macromolecular Structure Shared Resource, which is supported in part by NIH CA054174.

[‡]Resonance assignments and relaxation data for Aps1Δ2−19 have been deposited in BioMagResBank (entry 15875).

*To whom correspondence should be addressed. Phone: (210)-567-3711. Fax: (210)-567-3719. E-mail: barnesl@uthscsa.edu.

[1]Abbreviations: Aps1, $Ap_{six}A$ hydrolase; Aps1FL, full-length protein; Aps1Δ2−19, Aps1 with residues 2−19 deleted; Aps1Δ2−31, Aps1 with residues 2−31 deleted; Ap_nA, diadenosine 5′,5‴-P^1,P^n-oligophosphate; IP_7, (*PP*-InsP_5) diphosphoinositol pentakisphosphate; IP_8, ([*PP*]$_2$-InsP_4) bisdiphosphoinositol tetrakisphosphate; Ddp1, diadenosine and diphosphoinositol polyphosphate phosphohydrolase 1; DIPP1, diphosphoinositol polyphosphate phosphohydrolase 1; IP_6, inositol hexakisphosphate; IP6K1, inositol hexaphosphate kinase 1; HEPES, *N*-(2-hydroxyethyl) piperazine-*N*′-ethanesulfonic acid; DTT, dithiothreitol; PCR, polymerase chain reaction; pSGAPS1, plasmid pSGA02 containing the *aps1* open reading frame; LB, Luria−Bertani; IPTG, isopropyl-*β*-D-thiogalactopyranoside; PMSF, phenylmethanesulfonyl fluoride; EDTA, ethylenediaminetetraacetic acid; HPLC, high performance liquid chromatography; BSA, bovine serum albumin; SDS, sodium dodecyl sulfate; TROSY, transverse relaxation optimized spectroscopy; HMM, hidden Markov matrix.

 Published on Web 05/22/2009

demonstrated that diphosphoinositol polyphosphates were better substrates *in vitro* on the basis of the values of the specificity constants for Ap_6A, Ap_5A, and IP_7 (*4*). *S. cerevisiae* Ddp1 (*4*), proteins of the *H. sapiens* DIPP family (reviewed in ref (*3*)), and murine DIPP3 (*15*) are the only other enzymes shown to have this particular dual substrate specificity.

Although Aps1 has affinity and activity toward both classes of substrates *in vitro*, the *in vivo* substrate(s) and function(s) for the enzyme remain to be definitively determined. Ingram et al. (*13*) attempted to identify the *in vivo* substrate by disrupting and overexpressing the *aps1* gene in *S. pombe*. The intracellular concentrations of IP_7 and an isoform of IP_7, $[PP]_2$-InsP_3, significantly increased in the *aps1*-disrupted strain, but there was no significant change in IP_8 or Ap_5A, while Ap_6A was undetectable (*13*). There were no detectable phenotypic changes in growth rate, cell morphology, sporulation, or mating. On the basis of these results, the authors concluded that Aps1 functioned *in vivo* to degrade IP_7 and the IP_7 isoform. However, there was no significant change in the intracellular concentrations of IP_7, the IP_7 isoform, or IP_8 in the *aps1*-overexpression strain, while the concentration of Ap_5A paradoxically increased (*13*), in spite of a 6-fold increase in Aps1 enzymatic activity (*13*). Additionally, overexpression of Aps1 resulted in phenotypic changes, which occurred predominately in cell morphology. The observed changes were most consistent with proposed roles of diphosphoinositol polyphosphates in protein trafficking necessary for cell wall synthesis (*13*).

Site-directed mutagenesis and enzymatic assays of numerous nudix hydrolases have shown that the nudix motif is the catalytic site and that the presence of one or more divalent cations, for example, Mg^{2+} or Mn^{2+}, is required for catalysis (*16*). Specifically, site-directed mutagenesis of Aps1 (*13*) and human DIPP1 (*14*) demonstrated the necessity of residues in the nudix motif for hydrolysis of Ap_6A and for the latter enzyme that the same residues affected the hydrolysis of Ap_6A, IP_7, and IP_8. Nudix hydrolases catalyze the hydrolysis of a wide variety of substrates, and it has been established that the residues required for substrate specificity are distinct, relative to those of the conserved catalytic nudix motif (*14*, *17*). Mutagenesis of residues in human DIPP1 distal to the nudix motif decreased the rate of hydrolysis of Ap_6A, IP_7, and IP_8 to different extents indicating substrate-specific roles for the residues (*14*). Dunn et al. (*17*) and Xu et al. (*18*) have identified subfamilies of nudix hydrolases based on distinct conservations in sequences outside the nudix motif. Determination of the structures of a variety of nudix hydrolases has revealed differences in substrate binding and mechanisms of catalysis. Although the enzymes function to hydrolyze different substrates, all contain the structurally similar loop−helix−loop nudix motif and characteristic $\alpha/\beta/\alpha$ structural features of the nudix hydrolase superfamily (*16*).

To better understand the basis of dual substrate recognition by Aps1 and gain knowledge about the structure of this unique subfamily of nudix hydrolases, we used NMR spectroscopy to determine the secondary structure, backbone dynamics, and ligand binding properties of Aps1Δ2−19. We report that the hydrolysis of Ap_6A is independent of the first 31 residues of Aps1 on the basis of the determination of the values of K_m and k_{cat} for N-terminal truncated forms of the enzyme. Additionally, we identified secondary structural elements that are consistent with those of other nudix hydrolases and a large flexible loop, which appears to be unique to Aps1. We also measured the binding-dependent perturbations of backbone amide ^1H and ^{15}N resonances of Aps1Δ2−19 and a catalytically deficient Aps1Δ2−19-E93Q mutant in the presence and absence of Mg^{2+} to locate residues involved in binding the two different classes of substrates. The residues involved in binding were mapped on three-dimensional structural models of Aps1Δ2−19, which were generated using homology modeling (*19*).

MATERIALS AND METHODS

Materials. Ap_6A and $[^3H]Ap_6A$ were synthesized from either ATP or [2,8-^{3}H]ATP (Amersham/Pharmacia), respectively, (*20*), purified by anion-exchange chromatography, and analyzed for purity by HPLC (*21*). The following materials were purchased from the indicated company: *E. coli* strain BL21 (DE3) (Novagen); carboxymethyl-Sepharose and sulfopropyl-Sepharose resins (Sigma); IP_6 (phytic acid) and hydroxylapatite resin (Calbiochem); and nickel-Sepharose HisTrap HP 5 mL column (Pharmacia/GE). The compositions of the buffers were as follows: sonication buffer, 50 mM sodium phosphate, pH 6.8, 10% glycerol, 1 mM PMSF, and 0.5 μg/mL each of leupeptin and pepstatin; buffer A, 50 mM sodium phosphate, pH 6.8, and 10% glycerol; buffer B, 50 mM sodium phosphate, pH 8.0, and 10% glycerol; buffer C, 50 mM Hepes, pH 6.5, 10% glycerol, 1 mM PMSF, 1 mM EDTA, 0.2 mM IP_6, and 0.5 mM DTT; buffer D, 10 mM sodium phosphate, pH 6.8, 10% glycerol, 0.2 mM IP_6, and 0.5 mM DTT; buffer E, 50 mM Hepes, pH 6.8, 10% glycerol, and 0.5 mM DTT; and buffer F, 100 mM sodium phosphate, pH 8.0, and 10% glycerol.

Cloning of His_{10}-Tagged aps1, aps1Δ2−19, and aps1Δ2−31. PCR primers for *aps1*FL, 5′-ggagatata*catatg*cttgaaaataacgg-3′ and 5′-cattatgcatcggatccttagttttc-3′; *aps1*Δ2−19, 5′-gtctacgg*catatg*gtgaaccgctcaatgacttctcgtg-3′ and 5′-atccggatcctagttttcctcttta-3′; and *aps1*Δ2−31, 5′-gtgaaggt*catatg*aaaaatcgattc-3′ and 5′-atccggatccttagttttcctcttta-3′ (Nde I and BamH I sites are italicized and underlined, respectively) were used to amplify the open reading frame of the *aps1* gene from the pSGAPS1 plasmid generated by Ingram et al. (*12*) from the plasmid pSGA02 (*22*). The PCR product was digested with Nde I and BamH I, gel purified, and subcloned into a His_{10}-tag modified pET15b vector denoted as pET15b10H. The vector was also digested and gel purified. The resulting amino-terminal His_{10}-tagged plasmids were denoted pET15b10H*aps1*FL, pET15b10H*aps1*Δ2−19, and pET15b10H*aps1*Δ2−31. FL denotes full-length Aps1, Δ2−19 denotes Aps1 with residues 2−19 deleted, and Δ2−31 denotes Aps1 with residues 2−31 deleted. The target gene from each construct was sequenced at the UTHSCSA DNA core facility.

Site-Directed Mutagenesis of Aps1Δ2−19. An E93Q mutant of Aps1Δ2−19 was prepared using the QuickChange II Site-Directed Mutagenesis Kit (Stratagene), according to the manufacturer's protocol. Two complementary mutagenic primers (5′-cgtgaaggttgggaaCaGggcggactagtgggtc-3′, for the sense strand), with a two-base mismatch (capitalized) for Glu93, were used to create the E93Q mutation from a modified pET15b plasmid containing 10 histidine residues and the *aps1Δ2−19* gene insert. The resulting plasmid, denoted pet15b10H*aps1Δ2−19-E93Q*, was sequenced at the UTHSCSA DNA core.

Expression and Purification. *E. coli* BL21 (DE3) cells were transformed, according to the manufacturer's protocol, with the pET15b expression construct, and a single colony was used to inoculate the LB medium containing 100 μg/mL ampicillin. The culture was grown at 37 °C to an $OD_{600\ nm}$ of 0.6. Subsequently,

the cells were shifted to a room temperature shaker, induced with 1 mM IPTG, and grown overnight (16 h). The cells were pelleted at 4 °C by centrifuging at 8950*g* for 15 min and frozen on dry ice. Frozen cell pellets were thawed and resuspended using a volume of sonication buffer that was three times the wet weight of the cells. The cells were sonicated on ice, and the resulting cell extract was centrifuged for 30 min at 43000*g*. With the exception of wild-type Aps1, which was dialyzed in buffer C, crude supernatant fractions were dialyzed in buffer A with the addition of 1 mM PMSF.

All chromatographic columns were equilibrated with appropriate buffer and constructed such that the protein did not exceed 4.5 mg/cm^3 resin, and the flow rates did not exceed 1 mL/min. Appropriate fractions were pooled on the basis of the 280 nm absorbance elution profile and/or Ap_6A hydrolase activity. The dialyzed crude supernatant of wild-type Aps1 was applied to a column of carboxymethyl-Sepharose resin equilibrated in buffer C and eluted with a linear gradient of 50−200 mM NaCl. Pooled fractions were concentrated under N_2 pressure in an Amicon unit at 4 °C with a PM-10 ultrafiltration membrane (Millipore) and dialyzed in buffer D. The concentrated and dialyzed sample was then applied to a column of hydroxylapatite resin equilibrated in buffer D and eluted with a linear gradient of 100−250 mM sodium phosphate in buffer D. Appropriate fractions were pooled, concentrated, and dialyzed in buffer E as described above. The resulting sample was applied to a column of sulfopropyl-Sepharose resin equilibrated in buffer E and eluted with a linear gradient of 250−500 mM NaCl. Appropriate fractions were pooled, dialyzed in buffer F, and concentrated. Stock solutions of 1 mg/mL protein with a final buffer concentration of 50 mM sodium phosphate, pH 8.0, and 50% glycerol were aliquoted and stored at −20 °C.

The crude supernatant fractions of His_{10}-tagged full-length and truncated forms of Aps1 were dialyzed in buffer A and applied to a column of carboxymethyl-Sepharose resin equilibrated in buffer A. Bound protein was eluted with a linear gradient that was generally between 250 and 600 mM NaCl. After elution, the appropriate fractions were pooled, concentrated if necessary, and dialyzed in buffer B. To prepare the dialyzed samples for nickel-Sepharose affinity chromatography, sodium chloride and imidazole were added to final concentrations of 100 mM and 10 mM, respectively, and the samples were filtered through a 0.2 μm syringe filter. Each carboxymethyl-Sepharose purified protein sample was subsequently purified on a nickel-Sepharose 5 mL HisTrap column that was equilibrated in buffer B with the addition of 0.1 M NaCl and 10 mM imidazole. Generally, a linear gradient from 150 mM to 500 mM imidazole in buffer B was used to elute the proteins at a flow rate of 0.6 mL/min. Appropriate fractions were pooled and concentrated. The nickel-Sepharose column was stripped with 50 mM EDTA, washed, and regenerated with 100 mM $NiSO_4$ between each purification.

Pooled column protein fractions and purified protein were subjected to electrophoresis on polyacrylamide gels under denatured protein conditions using the discontinuous buffer system described by Laemmli (*23*) and modified by Studier (*24*).

Enzymatic Assays. The activity of full length and mutated forms of Aps1 were assayed with Ap_6A as substrate. During purification, a coupled enzyme assay was used to determine activity of the elution fractions as described by Ingram et al. (*12*). The assay is based on the hydrolysis of Ap_6A to major products ADP and p_4A, where ADP is a substrate for pyruvate kinase, and the oxidation of NADH by lactate dehydrogenase is measured by the change in absorbance at 340 nm. The minor product, ATP, generated by the symmetrical cleavage of Ap_6A by Aps1 (*12*) is not measured in the assay.

To determine the kinetic parameters for the different forms of Aps1, [^{3}H]Ap_6A was incubated in the presence of 50 mM Hepes, pH 8.0, 1 mM $MnCl_2$, and 50 μg/mL BSA, at 37 °C and in the presence and absence of enzyme. Each assay was stopped with a solution containing EDTA, and the residual substrate was removed from the reaction products (*12*) by chromatography on boronate resin (*25*). The collected reaction products were placed in a scintillation counter for data collection. In preliminary experiments, the enzymatic activity was determined to be a linear function of time and mass of protein under the assay conditions described above. Substrate saturation assays were conducted such that the substrate concentrations ranged from about 10-fold below and above the value of the K_m of the enzyme. The assays for wild-type Aps1, His_{10}-tagged Aps1FL, Aps1Δ2−19, and Aps1Δ2−31 were conducted between 0.3 μM and 50 μM [^{3}H]Ap_6A. Values for the kinetic parameters were calculated by an arbitrary weighted, chi-square minimization fitting of the data to the Michaelis−Menten equation using Origin software (*26*). The data were also fitted to the Eadie-Hoffstee plot using Excel software to detect any deviation from the Michaelis−Menten equation. The data were corrected when hydrolysis of the substrate exceeded 10% using equations described by Lee and Wilson (*27*). A two-tailed *t*-test assuming unequal variances was used to determine if there was a statistically significant difference among the kinetic parameters. A *P*-value of < 0.05 was considered statistically significant.

Preparation of Isotopically Labeled His_{10}-Tagged Aps1Δ2−19 and Aps1Δ2−19-E93Q Samples. Uniformly labeled ^{15}N, ^{13}C-^{15}N, or ^{2}H-^{13}C-^{15}N samples of His_{10}-tagged Aps1Δ2−19 and Aps1Δ2−19-E93Q for NMR spectroscopy were prepared by first growing a single colony of transformed *E. coli* in LB or in M9 minimal media that contained $^{15}NH_4Cl$ (1 g/L) and 100 μg/mL ampicillin. The culture was grown at 37 °C to an $OD_{600\ nm}$ of 0.6. The cells were pelleted by centrifuging at 8950*g* for 15 min, and media was discarded. The pelleted cells obtained from the culture grown in LB were washed with 0.5 × M9 salts solution, pelleted, and resuspended in M9 minimal media (*28*) that contained either $^{15}NH_4Cl$ (1 g/L) or $^{15}NH_4Cl$ and [^{13}C]-D-glucose (3 g/L), or $^{15}NH_4Cl$ and [^{13}C]-D-glucose in the presence of 99.9% D_2O. The cells were shifted to a room temperature shaker and allowed to equilibrate in the M9 minimal media for 1 h or for 1.5 h with minimal media containing D_2O. After the cells were equilibrated, 2.5 mL of 20% glucose or ^{13}C-D-glucose, as appropriate, was added, and the cells were induced with 1 mM IPTG and grown overnight (16 h) at room temperature. The cells were pelleted at 4 °C by centrifuging at 8950*g* for 15 min and frozen on dry ice. Selectively labeled samples were prepared using media containing unlabeled NH_4Cl and unlabeled amino acids, except for ^{15}N-labeled lysine or ^{15}N-labeled leucine (CIL, Woburn, MA), at concentrations described by Davis et al. (*29*). Protein samples were purified as described above, but were concentrated with a 10,000 molecular weight cutoff centrifugal filter (Millipore, Billerica, MA) and dialyzed in 25 mM sodium phosphate, pH 6.4, and 0.02% azide by removing glycerol in a stepwise fashion. The resulting protein concentrations ranged from 0.4 mM to 1.4 mM in different preparations.

NMR Spectroscopy. All NMR experiments were performed at 27 °C on Bruker 600 or 700 MHz spectrometers equipped with

either cryogenically cooled (600 MHz, 700 MHz) or conventional (700 MHz) 5 mm ^{1}H probes equipped with a ^{13}C and ^{15}N decoupler and pulsed field gradient coils. ^{1}H-^{15}N HSQC spectra were recorded using a conventional ^{1}H-^{15}N HSQC pulse sequence with water flipback pulses (*30*). All spectra were processed using NMRPIPE (*31*) and analyzed using the program NMRView (*32*) or NMRDraw (*31*).

Resonance Assignments. Backbone resonance assignments of His_{10}-tagged Aps1Δ2−19 were obtained by collecting and analyzing data from a standard 3D C(CO)NH experiment as applied to a protonated ^{13}C-^{15}N sample and TROSY-based HNCA, HNCACB, HN(CO)CACB, HNCO, and HN(CA)CO experiments as applied to a deuterated ^{13}C-^{15}N sample (*33*, *34*). Additionally, ^{1}H-^{15}N HSQC spectra of specifically ^{15}N-labeled lysine and ^{15}N-labeled leucine preparations of His_{10}-tagged Aps1Δ2−19 were collected and analyzed. Resonances are labeled according to the primary sequence of wild-type Aps1, and labels −23 to 0 represent the His_{10}-tag and linker sequence.

Secondary Structure of Aps1Δ2−19. NMR chemical shift values were used to determine the secondary structure of Aps1Δ2−19 by utilizing PECAN (protein energetic conformational analysis from NMR chemical shifts) software, which is accessible via an interactive server (*35*). Both primary sequence and assigned chemical shifts, specifically C^{α}, C^{β}, H^{N}, N, and C^{O}, of Aps1Δ2−19 were provided to PECAN, which chooses the best three chemical shift values based on a given residue, to determine a probability for the secondary structure (*35*).

Backbone ^{15}N Relaxation Parameters. Backbone amide ^{15}N T_1, ^{15}N T_2, and ^{15}N-{^{1}H} NOE relaxation data sets of ^{15}N-labeled His_{10}-tagged Aps1Δ2−19 were recorded in an interleaved manner at 27 °C at a magnetic field strength of 14.1 T (corresponding to ^{15}N frequency of 60.81 MHz) using ^{1}H-detected pulse schemes as described (*36*). The T_1 and T_2 data sets were colleted using 10 delay times, which varied between 16 and 3200 ms and 8−240 ms, respectively. The T_1 and T_2 relaxation times were obtained by fitting relative peak heights as a function of T_1 or T_2 delay time to a two-parameter exponential $I(t) = I_o \exp(-R_{1,2}\, t)$, where R_1 and R_2 are equal to $1/T_1$ and $1/T_2$, respectively (*37*). The errors in individual T_1 and T_2 measurements were estimated by Monte Carlo simulations (*38*). NOE values were obtained by taking the ratio of peak intensities from experiments performed with and without ^{1}H presaturation and by applying a correction to take into account the incomplete recovery of both ^{15}N and ^{1}H magnetization (*39*).

The relaxation data mean values and standard deviations were calculated to identify dynamic regions of the protein. R_2/R_1 values more than a standard deviation below the mean, which indicate dynamic regions of the protein, were not included in the calculation to determine the baseline mean (*40*).

Structural Modeling. NMR spectroscopy of Aps1Δ2−19 resulted in weak spectral data for some residues, which was likely due to exchange broadening and, hence, was insufficient for complete structure determination. Use of higher concentrations of protein was not possible because of protein precipitation. Therefore, we used structural homology modeling to corroborate and complement our NMR spectroscopic data to predict the three-dimensional structure of Aps1. In particular, homology modeling facilitated the identification of the position of residues potentially involved in binding ligands. Homology modeling based on known protein structures is widely used in conjunction with new structural data on proteins to predict the structure of the latter (*41*−*43*).

The primary sequence of Aps1 was obtained from the databank at the National Center for Biotechnology Information (http://www.ncbi.nlm.nih.gov/). Residues 2−19 were removed from the primary sequence of Aps1 *in silico*. The resulting sequence, designated Aps1Δ2−19, was submitted to the HHpred interactive server (*19*), which is one of the highest scoring servers among those tested for the CASP7 (critical assessment of techniques for protein structure prediction) experiments (*44*). Subsequently, the server generated a list of templates and query-template alignments by HMM (hidden Markov matrix) profiling (*45*). We chose the human homologue DIPP1 (PDB ID: 2FVV) as the structural template because it scored the highest in the query-template alignment and because of its overlapping dual substrate specificity with Aps1 (*4*). In addition, we chose Ndx1 (PDB ID: 1VC8), an Ap_6A hydrolase from *T. thermophilus*, as a structural template since the structure of the enzyme−Ap_5 complex had been determined. The percent identity and percent conservative substitution for each template sequence alignment to Aps1Δ2−19 were 28% and 57% for DIPP1, respectively, and 33% and 48% for Ndx1, respectively. The percents were calculated by dividing the number of identical pairs or the number of conservative substitutions (including identical pairs) by aligned positions (excluding gaps), which is most consistent with results obtained from the HHpred server (*19*). The resulting query-template alignments were individually provided to the MODELLER component of the HHpred server, and structural models of Aps1Δ2−19 were created on the basis of the satisfaction of spatial restraints derived from either template. The quality of each model was assessed by internal checks that include the stereochemistry of each model (e.g., bond angles, dihedral angles, and nonbonded atom−atom distances) (*46*). If inconsistencies were detected, MODELLER optimized the model until the spatial restraints were best satisfied (*46*). The program Contact (*47*) was used to determine the residues of DIPP1 and Ndx1 that are involved in binding IP_6 or Ap_5, respectively. We assumed a maximum distance of 5 Å in identifying potential residues involved in binding.

Titrations of Aps1Δ2−19 and Aps1Δ2−19-E93Q. Both Aps1Δ2−19 and Aps1Δ2−19-E93Q proteins were titrated with increasing concentrations of $MgCl_2$, Ap_6A, or IP_6, which were buffered in 25 mM sodium phosphate, pH 6.4, and 5% D_2O. Titrations of Aps1Δ2−19 with Ap_6A were carried out in the presence of 1 mM EDTA, and all other titrations, with the exception of $MgCl_2$, were carried out in the presence of 15 mM $MgCl_2$. Increasing concentrations of ligand ranging from 0 to 60 mM $MgCl_2$ over 17 steps, 0−1.17 mM Ap_6A over 12 steps, or 0−3 mM IP_6 over 12 steps were added to 350 μL of 0.27 mM protein solution, and a ^{1}H-^{15}N HSQC spectrum of the protein at each ligand concentration was recorded.

The perturbations of backbone amide hydrogen and amide nitrogen chemical shifts for assigned residues, which displayed observable, nonoverlapped resonances (146 of 160 assigned residues), were monitored as a function of increasing ligand concentration, and the weighted average chemical shift change was calculated using the following equation.

$$\Delta_{av} = \sqrt{(\Delta HN^2 + (\Delta N^2/25))/2} \qquad (1)$$

Using this equation, the maximum weighted average chemical shift change, Δ_{max} (ppm), was calculated on the basis of initial and final concentration points and plotted as a function of residue number. Chemical shift perturbations were considered

significant if they exceeded 0.07 ppm, which is based on the equation described by Hajduk et al. (*48*) and modified such that the weighted average chemical shift perturbation is considered (*49*). Dissociation constants for each residue exhibiting a significant chemical shift perturbation were determined by nonlinear least-squares fitting of the Δ_{av} values to the equation described by Kingston et al.

$$\Delta_{obs} = \frac{\boldsymbol{\delta}_b - \boldsymbol{\delta}_f}{2P_T}[(P_T + L_T + K_d) - \sqrt{(P_T + L_T + K_d)^2 - 4P_T L_T}] \quad (2)$$

where Δ_{obs} is the average observed chemical shift change, P_T and L_T are the total concentrations of protein and ligand, respectively, $(\delta_b - \delta_f)$ is the total chemical shift difference between the bound and the free state, and K_d is the equilibrium dissociation constant (*50*). Origin software was used for nonlinear least-squares fitting, and ± indicates parameter errors that are equal to the square root of the covariance matrix diagonal values (*26*). The effect of dilution was taken into account in the calculations.

RESULTS

Multiple Sequence Alignment of S. pombe Aps1 and Orthologues. A multiple sequence alignment of *S. pombe* Aps1 with *S. cerevisiae* Ddp1 and other putative fungal orthologues was generated to explore areas of potential interest, i.e., conservations, insertions, or deletions (Figure 1A). On the basis of the alignment, we constructed two N-terminal truncations. The first removed residues 2−19, which lack conservation among the orthologues and, in addition, removed an Asn-Gly dipeptide (residues five and six) that has a propensity to undergo deamidation, which results in isomeric protein forms (*51*). The second removed residues 2−31, which include three conserved basic residues, namely, arginine, that could potentially interact with the negatively charged phosphates of the substrates. The sequence alignment also revealed an apparent insertion in *S. pombe* Aps1 relative to Ddp1 and other putative fungal orthologues.

Purification of Wild-Type Aps1, His_{10}-Tagged Aps1, and Truncated Forms of Aps1. We purified wild-type Aps1 using sequential column chromatography with carboxymethyl-Sepharose, hydroxylapatite and sulfopropyl-Sepharose resins. The His_{10}-tagged forms of Aps1, full-length, Δ2−19, and Δ2−31, were purified by sequential column chromatography on carboxymethyl-Sepharose and nickel-Sepharose resins. The proteins behaved similar to one another during the purification process with the exception of the 2−31 truncated form of Aps1, which was less stable than the other forms of Aps1. For example, it precipitated quite readily during concentration processes and apparently lost enzymatic activity during storage at −80 °C. Therefore, we stored all protein preparations used for kinetic analysis in a buffered solution of 50 mM sodium phosphate, pH 8.0, and 50% glycerol at −20 °C to maintain stability. The protein concentration was sufficiently high so that the glycerol was diluted out for enzymatic assays.

Protein fractions were subjected to electrophoresis on 15% polyacrylamide−SDS gels and stained with Coomassie blue to monitor the purification process. The His_{10}-tagged proteins have an additional 24 amino acid residues, due to the N-terminal 10-histidine residue tag and the linker, in comparison to wild-type Aps1. These additional 24 residues, as well as the effect of the deleted residues in the truncated forms of Aps1, were reflected in the relative mobilities of the purified proteins on a SDS gel. The four different purified forms of Aps1 were estimated to be greater than 95% homogeneous on the basis of the patterns on the SDS gels (data not shown).

Kinetics. To ascertain if removal of residues 2−19 and residues 20−31 from Aps1 affected the hydrolysis of Ap_6A, the Michaelis constant (K_m), the catalytic constant (k_{cat}), and the specificity constant (k_{cat}/K_m) were determined for wild-type, His_{10}-tagged full-length, and the truncated forms of Aps1 (Table 1). Although it was unlikely that the His_{10}-tag would affect the kinetic properties of Aps1, we performed control assays and compared wild-type and His_{10}-tagged, full-length Aps1 to determine if the tag significantly changed any of the kinetic parameters. There were no significant differences in values of the kinetic parameters for wild-type and the His_{10}-tagged, full-length forms of Aps1 (Table 1). Analyses of our results indicate that there were no statistical differences in the values of the kinetic parameters for Aps1Δ2−19 and Aps1Δ2−31 versus full-length Aps1. We conclude that residues 2−31 of Aps1 do not significantly affect the binding or hydrolysis of Ap_6A.

The kinetic parameters we determined using the tritiated Ap_6A assay for wild-type Aps1 differ from the kinetic parameters previously reported for Aps1 (*12*). The previous assay method was based on HPLC analysis of the reaction products. Relatively, the values of K_m, k_{cat}, and, k_{cat}/K_m for Ap_6A hydrolysis were respectively 7-, 3-, and 2-fold higher than the corresponding values in the present study (*12*). The difference in parameters is likely due to the difference in methods since the tritiated assay is more sensitive than the HPLC assay. It may also reflect a difference in terms of sample preparation since the chromatographic procedures have been modified since Aps1 was first characterized (*12*).

NMR Assignments. We chose to determine the sequential backbone resonance assignments for His_{10}-tagged Aps1Δ2−19. This truncated form of Aps1 lacks residues 2−19 and an Asn-Gly dipeptide, residues 5 and 6, sequence that has a propensity to undergo deamidation (*51*). In addition, Aps1Δ2−19 appeared to have greater stability than Aps1Δ2−31 as indicated above. The Aps1Δ2−19 sample was initially analyzed by recording a ^1H-^{15}N heteronuclear single quantum coherence (HSQC) spectrum. The HSQC revealed a combination of well-dispersed peaks, indicating a structurally ordered protein, as well as a number of overlapping peaks in the random coil region, which is not uncommon for a protein of this size (24,444 kDa, including the His_{10}-tag and linker) (Figure 2A). The sequential backbone resonance assignments were determined using a suite of TROSY-based three-dimensional triple resonance experiments (see Materials and Methods) applied to samples of ^{13}C-^{15}N-Aps1Δ2−19 deuterated to a level of about 70%. To aid in the assignments and to identify residues initially difficult to identify due to spectral overlap, selectively labeled ^{15}N-lysine and ^{15}N-leucine samples were prepared, and subsequent HSQC spectra were collected (Figure 2B,C). The selectively labeled samples also confirmed the assignment of leucine and lysine residues previously assigned with the uniformly ^{15}N-labeled protein sample. A total of 183 residues are theoretically assignable. This number excludes prolines and the non-native N-terminal His_{10}-tag + linker. One hundred sixty residues, (87%), including partial assignments, have been assigned (Figure 2A). Unassigned residues were largely due to severe overlap or weak spectral data, likely caused by either rapid amide exchange or exchange broadening. One non-lysine residue, which is likely a metabolic product

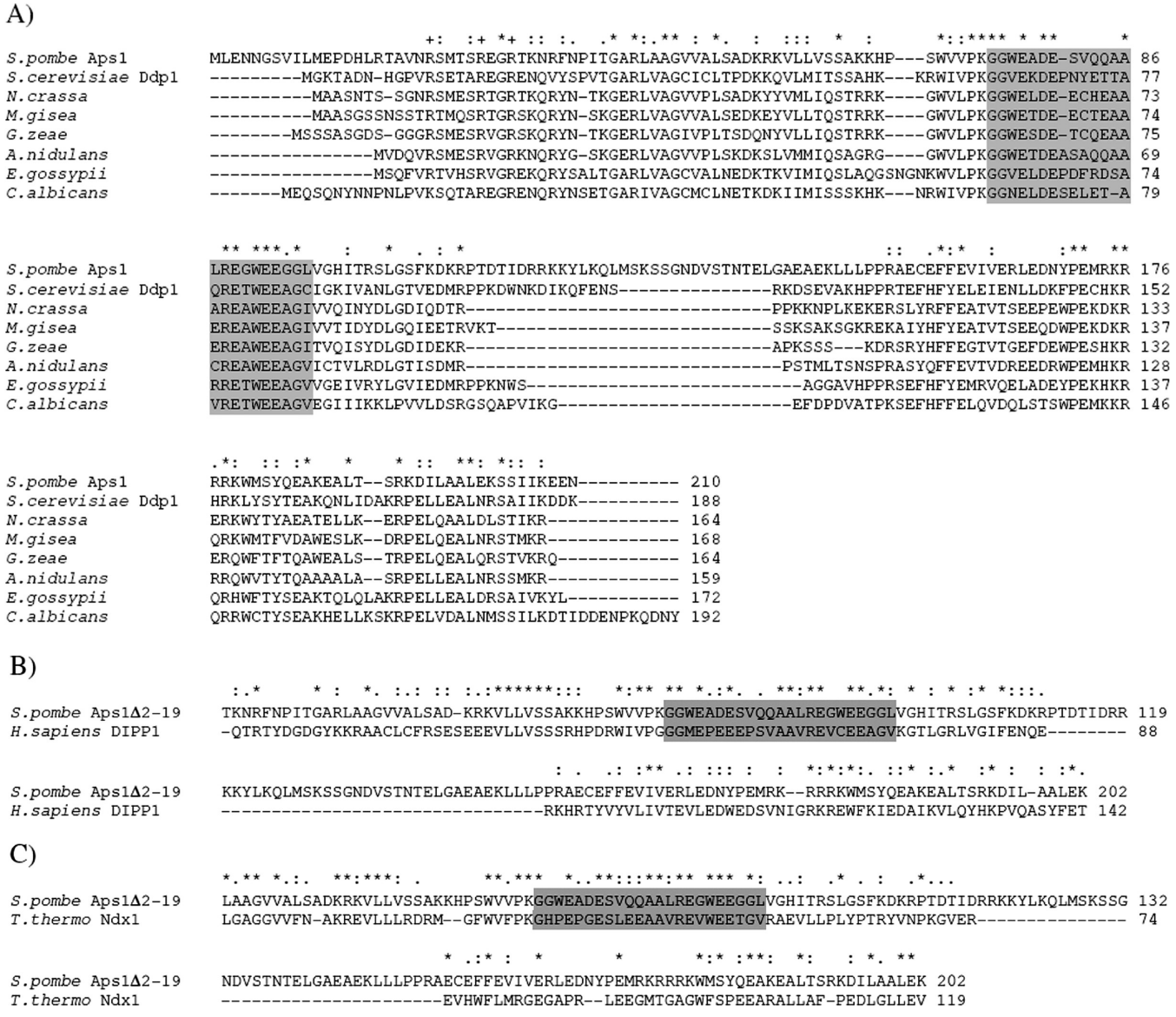

FIGURE 1: (A) Multiple sequence alignment of *S. pombe* Aps1, *S. cerevisiae* Ddp1 and putative fungal orthologues generated using Clustal X 1.8 (*66*). Sequence alignment of Aps1Δ2−19 with (B) DIPP1 and (C) Ndx1, based on Hidden Markov Matrix profiling (*45*), generated by the HHpred structural homology server (*19*). The numbering scheme is based on wild-type sequences of each protein. The region of the nudix motif is highlighted in gray. Notations: (+) conserved basic residues in the N-terminal region (residues 1−31) of Aps1; (*) indicates positions that have a single, fully conserved residue; (:) indicates conserved substitutions; (.) indicates semiconserved substitutions.

Table 1: Kinetic Parameters for the Hydrolysis of Ap_6A by Aps1 and the Truncated Forms of Aps1[a]

sample	K_m (μM)	k_{cat} (s^{-1})	k_{cat}/K_m ($M^{-1}s^{-1}$) × 10^5
WT Aps1	2.84 ± 0.45	0.67 ± 0.15	2.37 ± 0.51
10HAps1FL	3.29 ± 0.88	0.69 ± 0.14	2.12 ± 0.24
10HAps1Δ2−19	2.22 ± 0.93	0.89 ± 0.13	4.67 ± 2.06
10HAps1Δ2−31	2.19 ± 0.84	0.46 ± 0.20	2.23 ± 0.78

[a] The hydrolysis of [^{3}H]Ap_6A by Aps1 and the truncated forms of Aps1 was assayed as described in Materials and Methods. Sample abbreviations are WT = wild-type Aps1; 10H = His_{10}-tag + linker; FL = full length Aps1; Δ2−19 = Aps1 with residues 2−19 deleted; Δ2−31 = Aps1 with residues 2−31 deleted. Values are the means ± the standard deviation (n = 4 assays) for each sample. The values exhibit no significant statistical differences.

of lysine, was observed in the HSQC spectrum of the selectively labeled lysine sample. A similar observation has previously been reported in an unrelated study (*52*).

Secondary Structure of Aps1Δ2−19. The secondary structure of Aps1Δ2−19 was determined, on the basis of the analysis of chemical shift data using PECAN software (*35*) (Figure 3). The secondary structure was composed of a total of seven β-strands and five helices. The data indicated that the N-terminal region of Aps1 was dominated by β-strands βA, βB, and βC, which correspond to residues 42−50, 55−61, and 68−74, respectively. These β-strands precede the nudix catalytic helix α1 and β-strands βD and βE, which correspond to residues 82−94, 95−99, and 103−106, respectively. A small helix (α1′) encompassing residues 121−126 correlates to a segment of an apparent insertion in *S. pombe* Aps1 relative to other putative fungal orthologues (Figure 1A). The C-terminal region of Aps1 was composed of two β-strands regions βF and βG (residues 155−163 and 176−182, respectively) and an intervening helix α2 (residues 170−174), which precede the terminal helix segments α3 and α4 (residues 183−192 and 194−202, respectively). These secondary structure features of Aps1 agree with known general architectures of nudix

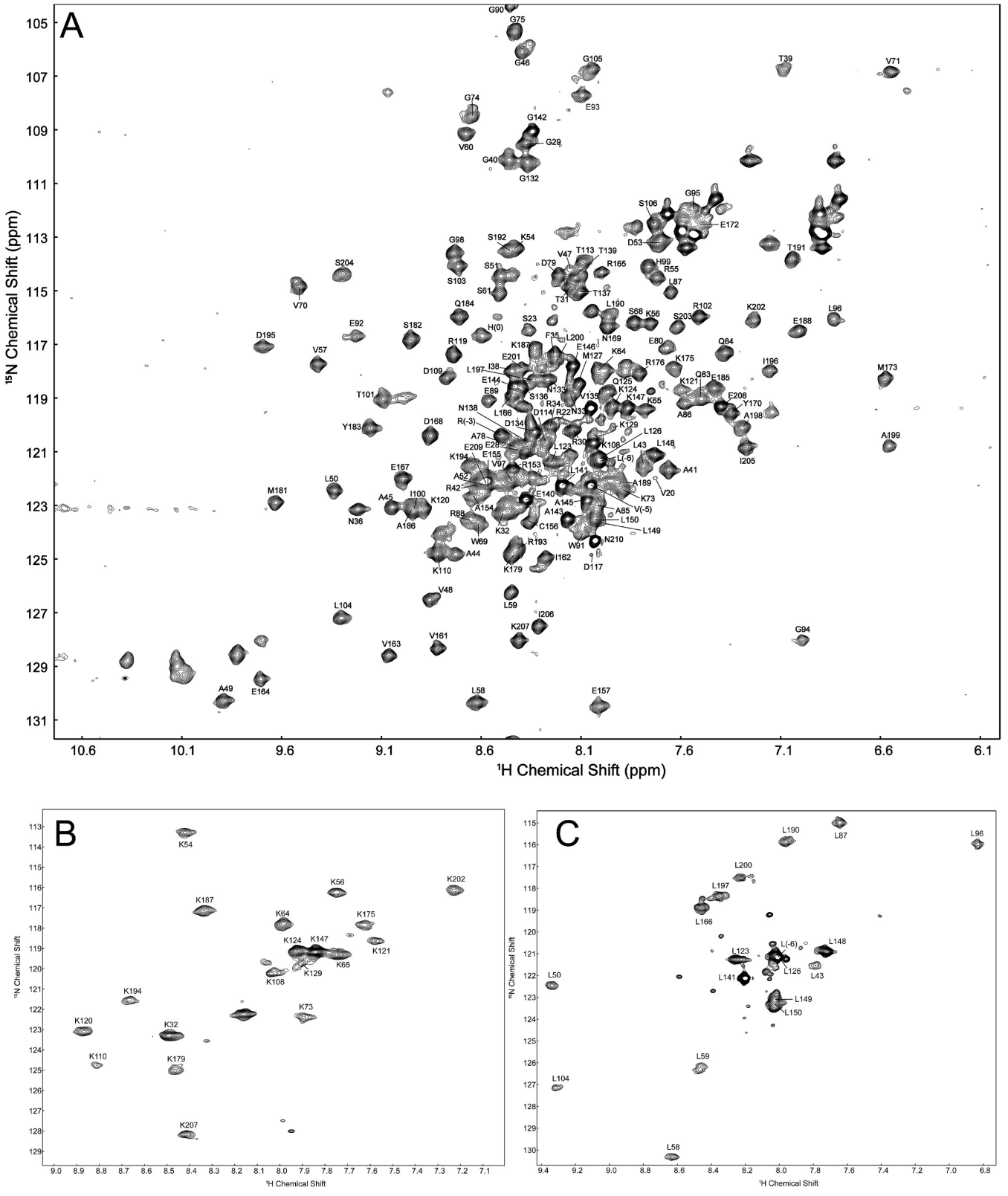

FIGURE 2: (A) Two-dimensional ^{1}H-^{15}N HSQC spectrum of 0.35 mM ^{2}H-^{13}C-^{15}N -labeled Aps1Δ2−19. (B) 2D-HSQC of 1.4 mM ^{15}N-lysine-Aps1Δ2−19 displaying 19 of 19 lysine residues and an apparent non-lysine residue at ^{1}H, 8.2 ppm, and ^{15}N, 122 ppm, which is likely a metabolic product of lysine. (C) 2D-HSQC of 1 mM ^{15}N-leucine-Aps1Δ2−19 displaying 18 of the 18 leucine residues. All samples were buffered in 25 mM sodium phosphate, pH 6.4, and 0.02% azide, and data were collected at 27 °C with a Bruker 600 or 700 MHz spectrometer. Peaks are labeled according to resonance assignments and are numbered according to wild-type Aps1. Residues −23 to 0 represent the His_{10}-tag and linker sequence.

hydrolases. For instance, the nudix motif box (residues 74−96) exhibits secondary structure elements that define a loop−helix−loop, which is a common structural characteristic for the nudix hydrolase family (*16*). In addition, the general secondary structure features of Aps1 display a α/β/α motif, which is also a defining characteristic of the nudix hydrolase family (*16*).

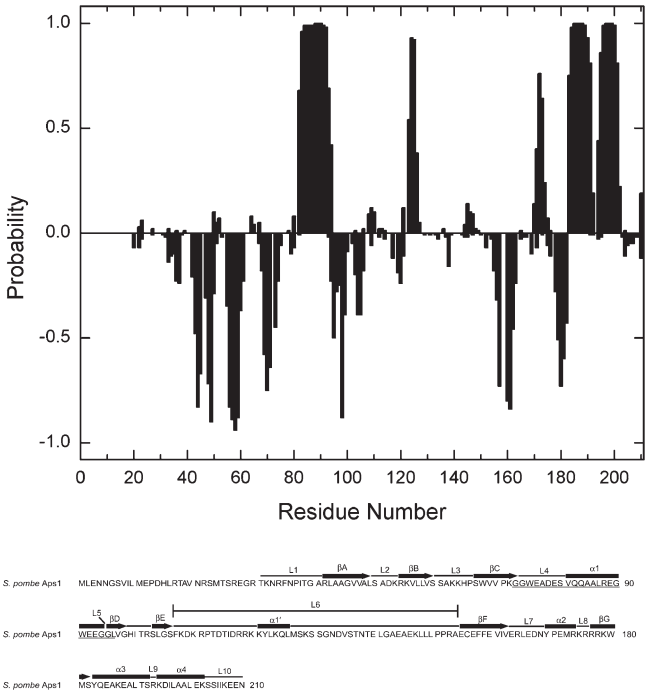

FIGURE 3: Secondary structure of Aps1Δ2−19 based on the analysis of chemical shift data with the PECAN program (*35*). The abscissa axis represents the residue number according to wild-type Aps1. The ordinate axis represents the probability for a given residue to participate in a helix (positive value) or in a β-strand (negative value). Values near zero represent residues designated as random coil. The sequence of Aps1 is labeled with the determined secondary structure for Aps1Δ2−19, which is consistent with the structural models of Aps1Δ2−19 (see Figure 5). α1′ is an α-helix that was identified by chemical shift analyses but was not present in the Aps1Δ2−19 structural model.

Backbone Dynamics of Aps1Δ2−19. The relaxation parameters ^{15}N R_1 ($1/T_1$), ^{15}N R_2 ($1/T_2$), and ^{15}N-{^{1}H} NOE were determined for Aps1Δ2−19 (Figure 4). The data indicated that Aps1Δ2−19 contains three dynamic regions. These regions were identified by values that deviate from the mean and standard deviation values of 0.77 ± 0.11, 0.78 ± 0.09 s^{-1}, and 32.7 ± 4.7 s^{-1} for NOE, R_1, and R_2, respectively. The mean values reflect an average that does not include the dynamic residues, as described in Materials and Methods. The first region, which is upstream of the nudix motif, encompasses residues 62−68. In this region, only residues, 64, 65, and 68, were associated with specific relaxation data. Data for neighboring residues were unavailable due primarily to complications in residue assignment (described above) or spectral overlap, which prevented reliable volume measurements of the assigned resonances. The second dynamic region encompassed residues 121−155, which correspond to the Aps1 sequence insertion relative to characterized homologues, *S. cerevisiae* DdpI and *H. sapiens* DIPP1 (Figure 1B) (*4*), respectively, and other putative fungal orthologues (Figure 1A). The third region corresponds to C-terminus residues 208−210. Together, the larger R_1, smaller R_2, and smaller NOE values, relative to calculated averages, for regions encompassing residues 62−68, 121−155, and 208−210 indicated increased flexibility on the picosecond to nanosecond time scale (*53*).

Homology Modeling of Aps1Δ2−19. The HHpred automated homology modeling server (*19*) was used to generate two structural models of Aps1Δ2−19 to gain additional insight in the structural architecture of Aps1Δ2−19 and to identify potential residues involved in binding each class of substrate. One model was generated based on the structure of the human homologue DIPP1 (PDB ID: 2FVV), which was shown to exhibit dual substrate specificity analogous to Aps1 (Figure 5A) (*4*). The other model, was generated on the basis of the structure of Ndx1 (PDB ID: 1VC8), a bacterial nudix hydrolase from *T. thermophilus*, which has been shown to hydrolyze Ap_6A (Figure 5B) (*54*). The models complement one another since each template structure was determined in the presence of a ligand reflecting the substrate specificity of Aps1, DIPP1 with IP_6, and Ndx1 with Ap_5. DIPP1 and Ndx1 have a sequence identity of 28% and 33% with Aps1Δ2−19, respectively, and conservative substitutions of 57% and 48% with Aps1Δ2−19, respectively (Figure 1B,C). On the basis of this sequence identity, each model is expected to be relatively accurate (*46*). In terms of model reliability, the stereochemistry of the final models were assessed with the program PROCHECK (*55*) and were determined to have greater than 98% of residues lie in the most favored or additionally allowed regions of the Ramachandran plot (data not shown).

The overall structural models of Aps1Δ2−19 generated with the MODELLER component of HHpred are in excellent agreement with the secondary structure determined by PECAN (Figure 5). It is evident from the models that specific features of nudix hydrolases, i.e., the catalytic helix, α/β/α sandwich motif, and two C-terminal helices, are present. However, one striking feature in the structural models of Aps1Δ2−19 is the large loops (loops L6 in Figure 5A,B). These loops stem from residues that do not align with the DIPP1 or the Ndx1 sequence and, therefore, could not be modeled on the basis of sequence homology. Data from the relaxation experiments (Figure 4) indicated that a majority of these residues exhibit dynamic behavior in solution. However, within this region there is a short α-helix as indicated by secondary structure determination (Figure 3).

Residues involved in binding IP_6 and Ap_5, within 5 Å, were identified in DIPP1 and Ndx1, respectively, by utilizing the program Contact (*47*), which computes distances of atom−atom contacts in protein structures. On the basis of these results, the potential residues of Aps1Δ2−19, which were most likely involved in binding IP_6 or Ap_5, were identified by the following criteria: the HMM sequence alignment between Aps1Δ2−19 and DIPP1 or Ndx1 (Figure 1B,C) and the proximity of the residues to the respective ligands in the structural models of Aps1Δ2−19. The results are shown in Table 2. Six residues, K64, G74, G75, E93, D109, and K194, appear to be common in potentially binding both classes of substrates.

^{1}H-^{15}N HSQC of Aps1Δ2−19 and the E93Q Mutant. To ascertain if the E93Q mutation affected any of the assigned amide nitrogen and amide proton resonances of Aps1Δ2−19 (Figure 2), a ^{1}H-^{15}N HSQC spectrum of Aps1Δ2−19-E93Q was overlaid with a ^{1}H-^{15}N HSQC spectrum of Aps1Δ2−19 (data not shown). The spectra indicated that residues G46, V48, S61, V71, E80, L87, E89, G90, W91, K129, and I162, most of which are located in the nudix motif and near the site of catalysis (*14*, *16*, *56*, *57*), were significantly affected by the E93Q mutation (Figure 6A). Ninety-three percent of the assigned backbone resonances of Aps1Δ2−19 remained unshifted in the Aps1Δ2−19-E93Q mutant (0.07 ppm threshold, see Materials and Methods).

Titration of Aps1Δ2−19 with $MgCl_2$. To investigate the residues potentially involved in binding Mg^{2+}, the perturbations of amide nitrogen and amide hydrogen chemical shifts for assigned residues of Aps1Δ2−19 were monitored as a function of increasing concentrations of $MgCl_2$. To identify residues

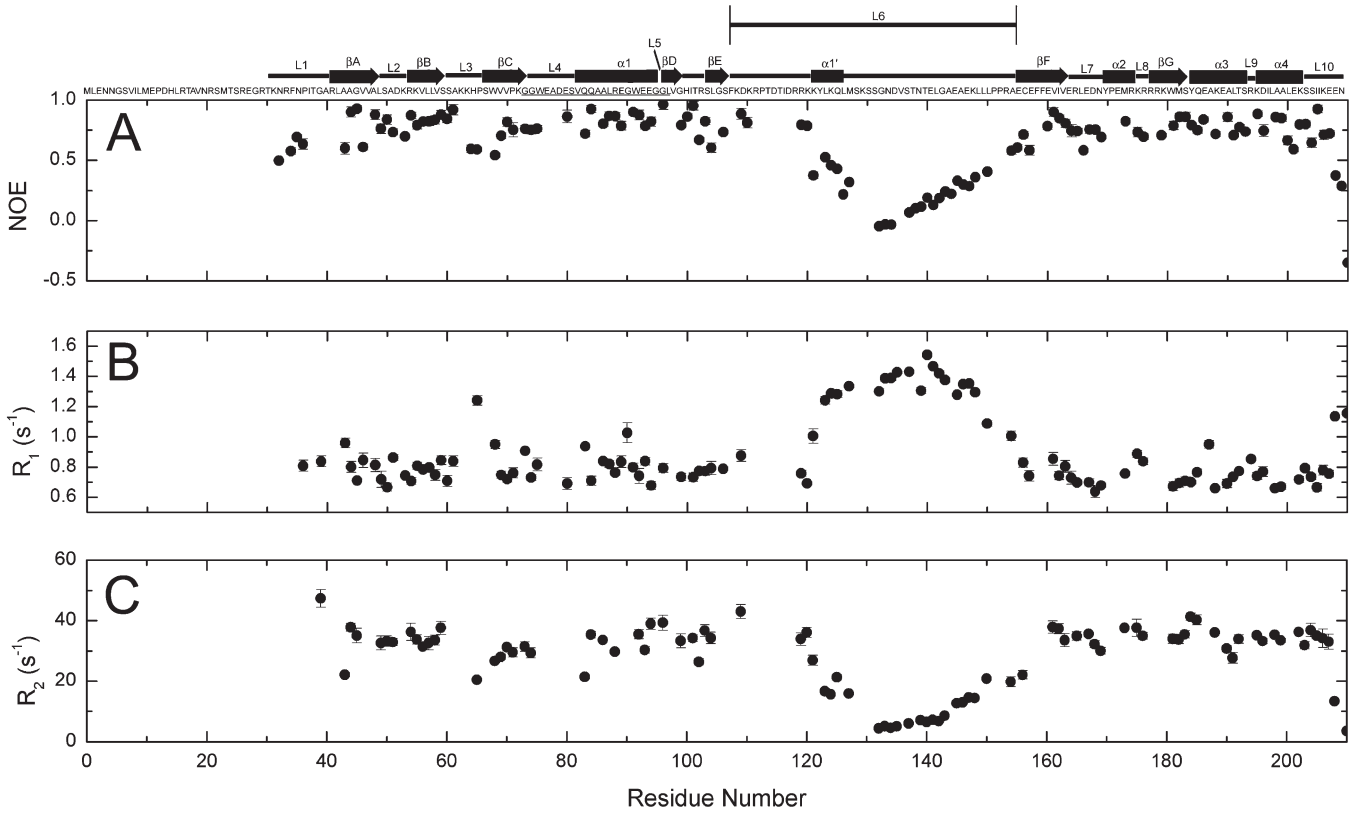

FIGURE 4: Backbone relaxation data for 1.4 mM ^{15}N-labeled Aps1Δ2−19 prepared in 25 mM sodium phosphate, pH 6.4, and 0.02% azide and collected at 27 °C with a Bruker 600 MHz ^{1}H spectrometer. (A) ^{1}H-^{15}N NOE values, (B) longitudinal relaxation rates, R_1, and (C) transverse relaxation rates, R_2. The larger R_1, smaller R_2, and smaller NOE values, relative to the corresponding mean value, for residues encompassing regions 62−68, 121−155, and the C-terminus indicate increased flexibility on the picosecond to nanosecond time scale (*53*). The secondary structure of Aps1Δ2−19 is shown above the panel with the NOE data.

exhibiting significant chemical shift perturbations, calculated values of maximum weighted average chemical shift change, Δ_{max}, were plotted as a function of residue number (Figure 6B). Subsequently, a dissociation constant, K_d^{Mg2+}, was determined for each residue exhibiting a significant chemical shift perturbation (see Material and Methods) by plotting the weighted average chemical shift change, Δ_{av}, as a function of ligand concentration. The majority of residues affected by the $MgCl_2$ titration exhibited nonspecific binding, as indicated by plots with a linear relationship, or were determined to have an apparent value of K_d^{Mg2+} that was greater than the final concentration of $MgCl_2$, thus resulting in an unreliable measure of K_d^{Mg2+}. Conversely, residues E93 and G74 of Aps1Δ2−19 exhibited specific binding of Mg^{2+} with dissociation constant K_d^{Mg2+}values of 5.1±0.54 mM and 26 ± 3.6 mM, respectively. E93 of Aps1Δ2−19 is equivalent in sequence to residues E70 and E57 of human DIPP1 and *E. coli* MutT, respectively. These glutamate residues have been shown to be essential for substrate catalysis and likely function as metal ligands (*10*, *57*). In addition, G74 of Aps1Δ2−19 is equivalent to residue G38 in *E. coli* MutT, which was identified as a potential metal ligand on the basis of Mn^{2+} binding studies (*57*).

The E93Q mutant has 3×10^{-4} times the hydrolase activity toward Ap_6A as compared to Aps1 (*13*). Although the activity of Aps1-E93Q has not been tested with respect to the diphosphoinositol polyphosphates, an equivalent E70Q mutant of the human homologue DIPP1 exhibited negligible activity toward diphosphoinositol polyphosphates (*4*), which suggests that Aps1-E93Q also has negligible activity toward diphosphoinositol polyphosphates. The E93Q mutation clearly effected Mg^{2+} binding (Figure 6C). This was evidenced by the lack of chemical shift perturbations exhibiting specific binding.

Titration of Aps1Δ2−19 with IP$_6$ and Ap$_6$A. Residues of Aps1Δ2−19 involved in binding IP_6 and Ap_6A were identified by titrating the enzyme with increasing amounts of ligand in the presence or absence of 15 mM $MgCl_2$ and monitoring the perturbation of the protein backbone amide nitrogen and amide hydrogen chemical shifts for assigned residues. The dissociation constant (K_d) was determined for each residue that exceeded the weighted average chemical shift perturbation threshold (Figure 6D,F) and that exhibited specific binding (Figure 7A and Table 3). The residues exhibiting specific binding were mapped on the surface of the Aps1Δ2−19 model generated with either a structural template of human DIPP1, which includes a bound IP_6 ligand (Figure 8A, center), or with a structural template of a bacterial Ap_6A hydrolase, Ndx1, which includes a bound Ap_5 ligand (Figure 8B, center). The residues predicted to most likely bind IP_6 or Ap_5, which are listed in Table 2, were mapped on the representative models of Aps1Δ2−19 in Figure 8A and B (left), respectively.

On the basis of the location of the residues exhibiting specific binding for IP_6 in the structural model of Aps1Δ2−19, K32, R34, G74, E93, and D109 appear to be the most consistent with residues predicted to bind IP_6 (Table 2 and Figure 8A, center). The other residues anticipated to bind IP_6 (Table 2) did not exhibit significant chemical shift perturbations; therefore, the values of K_d were not determined. No data were available for residue R42 since this residue was not assigned. In addition to identifying residues anticipated to bind IP_6, other unexpected residues were identified. These residues, M127, K147, and L148,

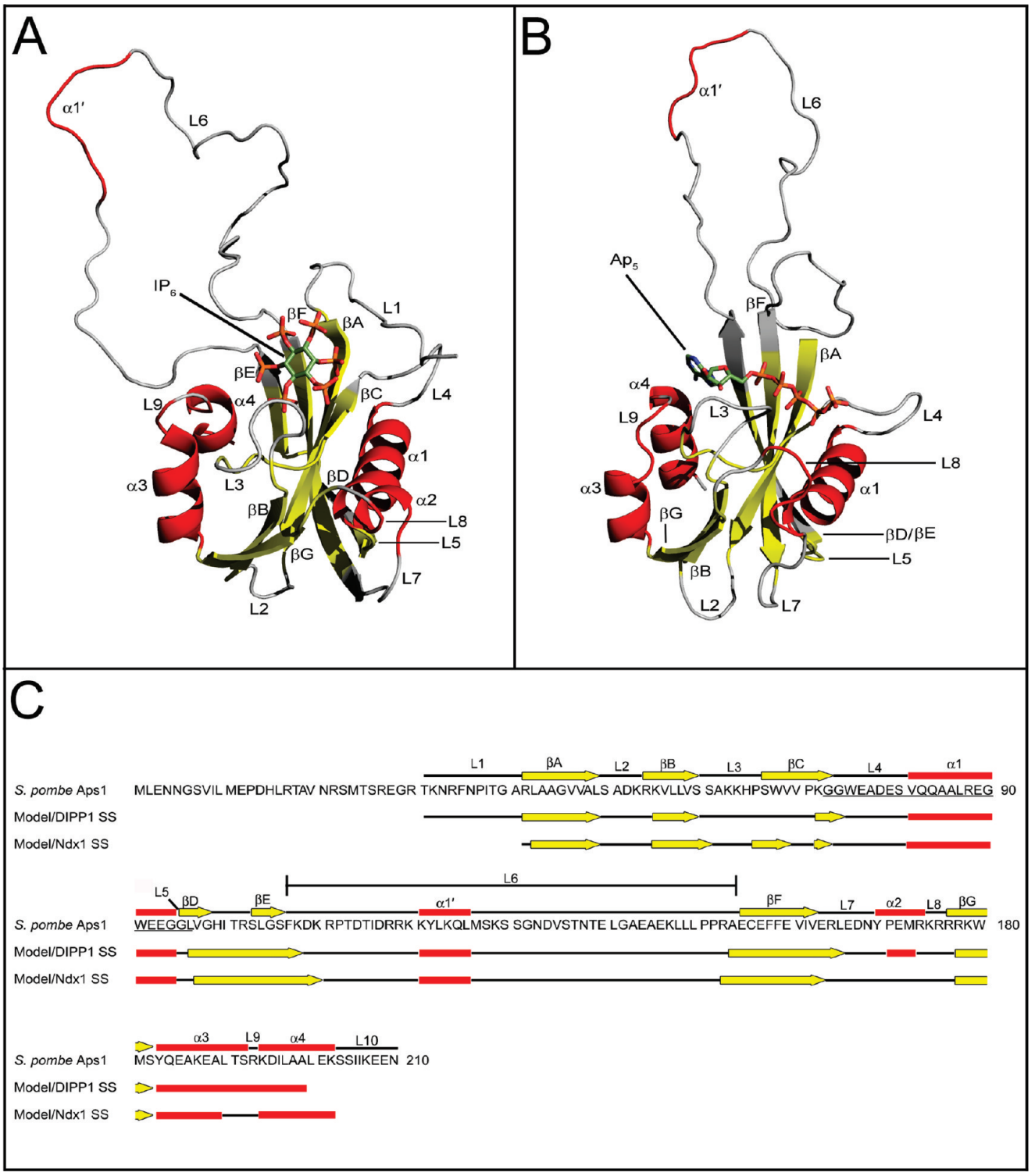

FIGURE 5: Structural models of Aps1Δ2−19 with IP_6 and Ap_5 ligands. Structural models of Aps1Δ2−19 generated by the HHpred homology modeling server using template structures of (A) the human homologue, DIPP1 (PDB ID: 2FVV), or (B) the Ap_6A hydrolase, Ndx1 (PDB ID: 1 VC8). IP_6 and Ap_5 are shown in the presumed binding site by superposing the ligand-bound structures of DIPP1 and Ndx1 with the Aps1Δ2−19 structural model, respectively. Loop (L6) corresponds to residues that did not align to either template sequence. Loop (L1), helix (α2), and β-strand (βC) are not present in the model generated with Ndx1. The color schemes on each model reflect the determined secondary structure based on chemical shift analyses with PECAN: red, helix; yellow, strand; and gray, coil. (C) Comparison of the NMR-derived secondary structure of Aps1Δ2−19 (above the sequence) to the DSSP generated (*67*) secondary structures of the Aps1Δ2−19 structural models (below the sequence).

can conceivably orient themselves near the ligand upon binding since they are located in the dynamic loop (L6) (Figure 8A, center).

To determine the residues involved in binding the dinucleotide substrate, Aps1Δ2−19 was titrated with increasing amounts Ap_6A in the presence of EDTA. The addition of EDTA extensively limits the hydrolysis of Ap_6A by chelating any free metals necessary for hydrolysis (*12*). On the basis of the location of the residues that exhibited specific binding on the Aps1Δ2−19 model (Figure 8B, center), residues K65, G74, and G75 are most consistent with residues predicted (Table 2) to bind the Ap_5 molecule based on the structural model (Figure 8B, left). The

Table 2: Residues in DIPP1 and Ndx1 That Bind IP_6 and Ap_5, Respectively, and the Corresponding Residues in Aps1Δ2−19 That Potentially Bind IP_6 and Ap_5, Respectively

IP_6		Ap_5	
DIPP1[a]	Aps1Δ2−19[b]	Ndx1[c]	Aps1Δ2−19[d]
R10	R34	M23	K64
K18	R42	K30	K73
R41	K64	G31	G74
G51	G74	H32	G75
G52	G75	E46	E89
E70	E93	E50	E93
N86	D109	Y66	D109 (F107)
R89	P152 (R153)	N68	R111
H91	A154 (R153)	E90	E172
R115	R176	F110	S192 (R193)
K133	K194	P111	K194
		E112	D195

[a,c] Amino acid residues in DIPP1 and Ndx1 identified to most likely bind IP_6 and Ap_5, respectively, based on the program Contact assuming a maximum distance of 5 Å (*47*). [b,d] Amino acid residues in Aps1Δ2−19 that potentially bind IP_6 and Ap_5 based on the HMM sequence alignment of Aps1Δ2−19 with DIPP1 or Ndx1 (Figure 1B,C) and the proximity of the residues to the respective ligands in the structural models of Aps1Δ2−19 (Figure 5A,B). Amino acids in parentheses are adjacent residues that may be involved in binding. Residues are numbered on the basis of the wild-type sequence of each protein.

other residues anticipated to bind Ap_5 did not exhibit significant chemical shift perturbations, and no data were available for residues F107, R111, and S192 since they were not assigned. Analysis of the titration data also revealed additional residues not expected to bind Ap_5. These residues were K121, L123, K124, M127, and L148, which are located in the large dynamic loop (L6) (Figure 8B, center). Representative binding curves for residues that exhibited specific binding of Ap_6A are shown in Figure 7B.

Kinetic analysis of site-directed mutants of residues G51, G52, and E70 in DIPP1, which are conserved as G74, G75, and E93, respectively, in Aps1Δ2−19 revealed a negligible rate of hydrolysis for diphosphoinositol polyphosphates and diadenosine oligophosphates (*14*). Kinetic analysis of a site-directed mutant of residue E50 in Ndx1, which is conserved as E93 in Aps1Δ2−19, revealed a negligible rate of hydrolysis of Ap_6A (*54*). The results of these two studies suggest a role for these residues in catalysis and/or ligand binding with the latter being supported by our study.

Titration of Aps1Δ2−19-E93Q with IP_6 and Ap_6A. To ascertain the residues involved in binding IP_6 and Ap_6A in the catalytically deficient Aps1Δ2−19-E93Q mutant, titrations were performed in the presence of 15 mM $MgCl_2$ to best simulate enzymatic catalysis. Analysis of the data revealed that residues K64, K65, G75, and K121 were among those identified to bind IP_6 (Figure 8A, right). These residues are the most consistent with the residues predicted to bind IP_6 (Figure 8A, left). Only two residues, K121 and R176, of Aps1Δ2−19-E93Q, exhibited specific binding for Ap_6A (Table 3). On the basis of the location of these residues in the structural model of Aps1Δ2−19, K121 could potentially be involved in binding since it resides in the dynamic loop (Figure 8B, right). R176, however, is positioned further away from the ligand, suggesting that it is indirectly involved in binding. The fact that only two residues exhibit specific binding for the E93Q mutant suggests that the mutation has a greater effect on binding Ap_6A as opposed to binding IP_6. The basis for this effect on Ap_6A binding is not known. However, one possibility is that the perturbation of residues induced by the E93Q mutation (Figure 6A) affected the conformation of the protein such that the magnitude of the perturbations upon binding Ap_6A were not significant as compared to binding IP_6. Potentially, this could be attributed to the fact that Ap_6A stretches toward the site of mutation, while the position of IP_6 is less intrusive at this site.

DISCUSSION

In this study, we determined the kinetic parameters of K_m, k_{cat}, and k_{cat}/K_m for the hydrolysis of Ap_6A by two N-terminal truncated forms of Aps1. The rationale for constructing the Aps1Δ2−19 and Δ2−31 N-terminal truncations were stated in the Results section. In addition, these parameters were determined for two full-length forms of Aps1, wild-type and Aps1 with the His_{10}-tag and linker, in order to establish a valid comparison among the different forms of Aps1. The kinetic data (Table 1) indicate that residues 2−31 of Aps1 do not participate significantly in the binding and hydrolysis of Ap_6A. Clearly, for Ap_6A, the residues responsible for substrate binding lie elsewhere in the sequence, or the binding is dependent on more than just the amino acids located between residues 2−31. Residues 2−31, especially 20−31, may be structurally important on the basis of our observation that Aps1Δ2−31 was more susceptible to precipitation during purification than wild-type Aps1 and Aps1Δ2−19. Aps1Δ2−19 was chosen for the subsequent structural studies for the reasons stated in the Results section (NMR assignments).

On the basis of NMR spectroscopic analyses of Aps1Δ2−19, we determined the secondary structure and the dynamic nature of specific regions of the enzyme. The secondary structural features (Figure 3) of a loop−helix−loop for the nudix motif box, a C-terminal helix−turn−helix, and β-strands, which are presumably sandwiched in between, describe the overall $\alpha/\beta/\alpha$ motif for the enzyme and agree with the common structural characteristic for the nudix hydrolase family (*16*). Relaxation data indicated that there are three flexible, dynamic regions in Aps1: residues 62−68, residues 121−155, and the C-terminal residues 208−210. Residues 62−68, which precede the nudix motif, constitute loop (L3) in the structural model of Aps1Δ2−19 and appear to form a portion of the binding pocket for the ligand (Figure 5A). Residues 121−155 represent the majority of a large insert in Aps1 relative to DIPP1 (Figure 1B) that behaves as a flexible loop in solution. Structurally, the loop contains a small helix ($\alpha1'$, residues 121−126) that was identified on the basis of chemical shift data (Figure 3). The large flexible loop, 34 residues, in Aps1 is somewhat surprising given the similar enzymatic properties of Aps1 and DIPP1 (*4*, *12*). Interestingly, dynamic studies conducted with an Ap_4A nudix hydrolase from *L. angustifolius* (PDB ID: 1JKN) indicate that it contains a dynamic loop similar in position to loop (L6) in the Aps1Δ2−19 model (*58*). However, the loop in *L. angustifolius* is 2.5 times shorter, contains a longer helix, and, in addition, contains a flexible region that corresponds to loop (L8) in the Aps1Δ2−19 model (Figure 5A). The function of the large loop in Aps1 is unknown. However, it is analogous in position to a small loop in the human homologue DIPP1, in which residues R89/H91 (Table 2) have been identified to bind IP_6. Similarly, Ndx1 has a small loop at this position, but the residues identified to bind Ap_5 (Y66/R74) appear to flank the loop on either side. The ligand binding data suggest a potential

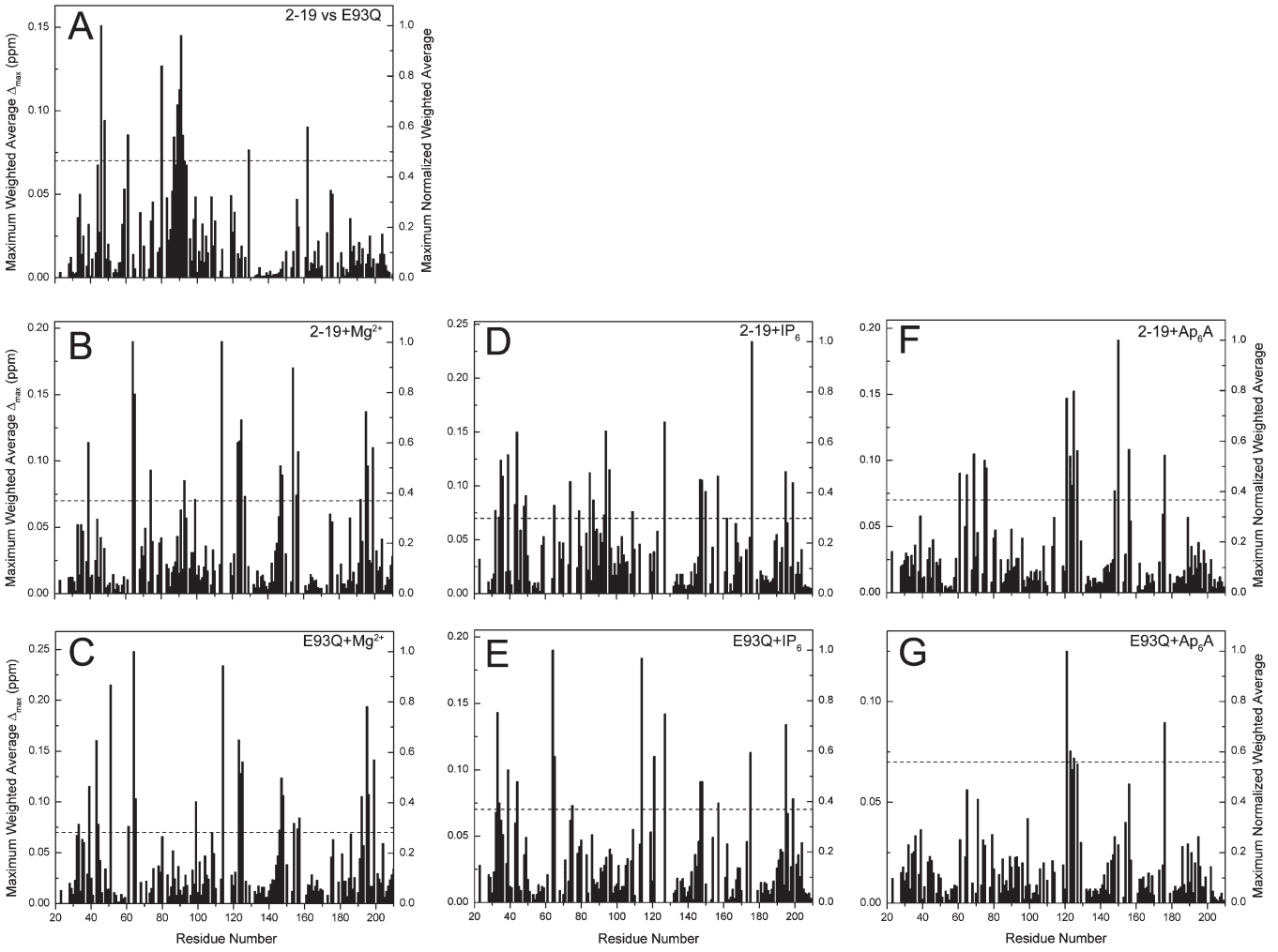

FIGURE 6: Backbone amide hydrogen and amide nitrogen weighted average chemical shift differences of Aps1Δ2−19 and an Aps1Δ2−19-E93Q mutant upon binding of Mg^{2+}, IP_6, or Ap_6A ligands. The maximum weighted average chemical shift difference, Δ_{max} (left ordinate axis), was calculated from chemical shift values obtained from ^1H-^{15}N HSQC spectra collected for initial (0 mM) and the indicated final concentration of ligand and plotted as a function of residue number (abscissa axis). The value of Δ_{max} exhibiting the greatest magnitude was used to normalize the data (right ordinate axis). (A) Chemical shift differences between Aps1Δ2−19 and Aps1Δ2−19-E93Q in the absence of ligands. (B) Chemical shift differences for Aps1Δ2−19 at 0 and 30 mM $MgCl_2$, (D) 0 and 3 mM IP_6, and (F) 0−1.17 mM Ap_6A. (C) Chemical shift differences for Aps1Δ2−19-E93Q at 0 and 60 mM $MgCl_2$, (E) 0 and 3 mM IP_6, and (G) 0 and 1.17 mM Ap_6A. The dashed line represents the threshold for significant chemical shift perturbation.

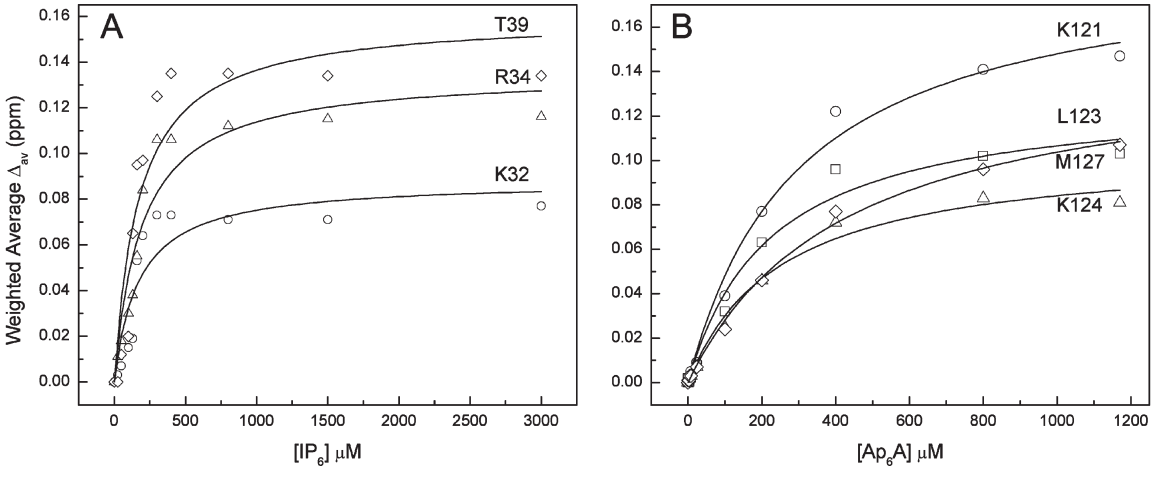

FIGURE 7: Representative binding curves that exhibit specific binding of IP_6 and Ap_6A in the presence and absence of $MgCl_2$, respectively, to Aps1Δ2−19. (A) Residues K32, R34, and T39 of Aps1Δ2−19 that exhibit specific binding for IP_6 in the presence of $MgCl_2$ and (B) residues K121, L123, K124, and M127 in Aps1Δ2−19 that exhibit specific binding of Ap_6A in the absence of $MgCl_2$. Weighted average chemical shift perturbations (*49*) are plotted as a function of increasing ligand concentration. Dissociation constants were determined by nonlinear least-squares fitting of the data to the equation described by Kingston et al. (*50*) with Origin software (*26*).

Table 3: Dissociation Constants[a] Determined for Residues in Aps1Δ2−19 or the Aps1Δ2−19-E93Q Exhibiting Significant[b] Chemical Shift Perturbations As a Function of Increasing Ligand Concentration

	Aps1Δ2−19		Aps1Δ2−19-E93Q	
	K_d^{IP6} (μM)	K_d^{Ap6A} (μM)	K_d^{IP6} (μM)	K_d^{Ap6A} (μM)
K32	172 ± 68			
N33			56 ± 30	
R34	191 ± 50		159 ± 44	
F35	161 ± 61			
N36	138 ± 49			
T39	173 ± 59		112 ± 31	
L43	208 ± 71			
A44	106 ± 60		124 ± 34	
V48	113 ± 47			
A49	167 ± 85			
S61		135 ± 45		
K64			105 ± 40	
K65		295 ± 48	88 ± 27	
W69		218 ± 42		
G74	278 ± 166	271 ± 45		
G75		312 ± 48	110 ± 31	
D79	112 ± 31			
A85	152 ± 61			
L87	79 ± 24			
E93	176 ± 61			
G94	107 ± 64			
L96	202 ± 94			
D109	114 ± 41			
D114			139 ± 63	
K121		298 ± 42	160 ± 38	364 ± 52
L123		223 ± 42		
K124		249 ± 40		
M127	218 ± 56	425 ± 40	154 ± 29	
K147	80 ± 39		104 ± 34	
L148	147 ± 58	458 ± 26	126 ± 34	
C156		435 ± 57		
E157	111 ± 33		130 ± 25	
K175			164 ± 30	
R176	510 ± 145	235 ± 34		57 ± 17
D195	108 ± 69		119 ± 43	
A199	107 ± 65		105 ± 34	

[a] The dissociation constants were determined by nonlinear least-squares fitting to the equation described by Kingston et al. (*50*). The parameter error (±) is equal to the square root of the covariance matrix diagonal values calculated using Origin software (*26*). All titrations were conducted in the presence of 15 mM $MgCl_2$ except for Aps1Δ2−19 with Ap_6A, which was conducted in the presence of 1 mM EDTA. [b] Perturbations are considered significant if the value of Δ_{max} exceeds the 0.07 ppm threshold (Materials and Methods).

role for this dynamic loop, which will be revisited in the latter part of the discussion. This is the first report of backbone dynamics for a nudix hydrolase exhibiting activity toward diadenosine oligophosphate and diphosphoinositol polyphosphate substrates.

We described structural models for Aps1Δ2−19 based on the human homologue DIPP1 and Ndx1, a bacterial Ap_6A nudix hydrolase. The models were generated using homology modeling, which is based on the idea that proteins with evolutionarily related sequences have similar three-dimensional structures and that structures diverge slower than sequences (*59*, *60*). Analysis of these models revealed several structural elements consistent with the experimental NMR data including the determined secondary structure and the large dynamic loop, which is unique to Aps1, on the basis of a comparison to known structures of other nudix hydrolases (*16*). In addition, the model agrees well with the general structure and structural characteristics observed for other members of the nudix hydrolase family (*58*, *61*, *62*). Furthermore, the residues of Aps1Δ2−19 presumed to bind IP_6 and Ap_5 were identified on the basis of the HMM sequence alignment between Aps1Δ2−19 and structural templates DIPP1 and Ndx1, which contain bound ligands (Table 2).

The residues involved in binding IP_6 and Ap_6A were determined by utilizing NMR chemical shift mapping in combination with structural modeling (*63*). The results demonstrate significant chemical shift perturbations for residues in and around the site predicted to bind IP_6 and Ap_5 (Figure 8A,B). There were some residues, R153 and K194, that were predicted to contact the IP_6 ligand but did not exhibit significant shift perturbations. Similarly, residues K64, E89, E93, D109, K194, and D195, which were predicted to contact the Ap_5 ligand, did not exhibit significant chemical shift perturbations. This is most likely due to the fact that the contacts with the ligand are made predominantly by the terminal groups of residue side-chains, and hence, the perturbations at the observed site, the backbone amide, are relatively minor. Interestingly, some residues in the dynamic loop were also perturbed, which suggests that it may play a potential role in binding the ligands. Perhaps loop residues facilitate ligand entry and/or exit in Aps1, which may be less critical in DIPP1 on the basis of the absence of the large loop. Another possibility is that the loop functions to orient the diadenosine oligophosphate substrate in the proper position for ultimately producing ADP + p_4A as a major product of hydrolysis, rather than 2 ATP or AMP + p_5A, which are the major products of the bacterial and human homologues, respectively (*4*, *12*, *54*). This is an area of interest for further exploration since the loop is unique to Aps1 among known homologues.

One must consider the possibility that some of the observed shift perturbations do not arise as a consequence of direct contacts with the ligand but indirectly through a network of interactions. The residues presented in Table 3 reflect both direct and indirect binding of the respective ligands. Specifically, residues K32, R34, K64, K65, G74, G75, E93, D109, and K147 are likely to directly bind IP_6 (Figure 8A; center, right), and residues K65, G74, G75, K121, and K124 (Figure 8B; center, right) are likely to directly bind Ap_6A since they likely stabilize the ligand or ligand−Mg^{2+} complexes through electrostatic interactions of their side-chain terminal groups or backbone carbonyl groups. In addition, residues most likely involved in indirect binding of the respective ligands are F35, N36, G94, and L148 for IP_6, and S61, W69, L123, and M127 for Ap_6A (Table 3) since they are not in the immediate proximity of the respective ligands, yet exhibit specific binding. Hence, they likely stabilize the ligand through indirect interactions. Though the majority of residues exhibiting chemical shift perturbations agree with the residues predicted to bind IP_6 or Ap_5 (Figure 8A,B; left), there were other residues that we were not able to identify *a priori* since the loop had no complementary sequence with the structural homologues. Nevertheless, we favor the idea that the residues identified in the loop orient themselves to bind the ligands since the loop is dynamic, and structural changes are not likely to be readily indirectly transmitted.

In addition to the charged residues anticipated to directly bind the respective ligands, residue F107 of Aps1Δ2−19 was anticipated to bind Ap_5 (Table 2) via ring stacking with the Ap_5 adenosine moiety, as suggested by the ring stacking observed for residues Y66 and F110 in the structure of Ndx1 (PDB ID: 1VC8).

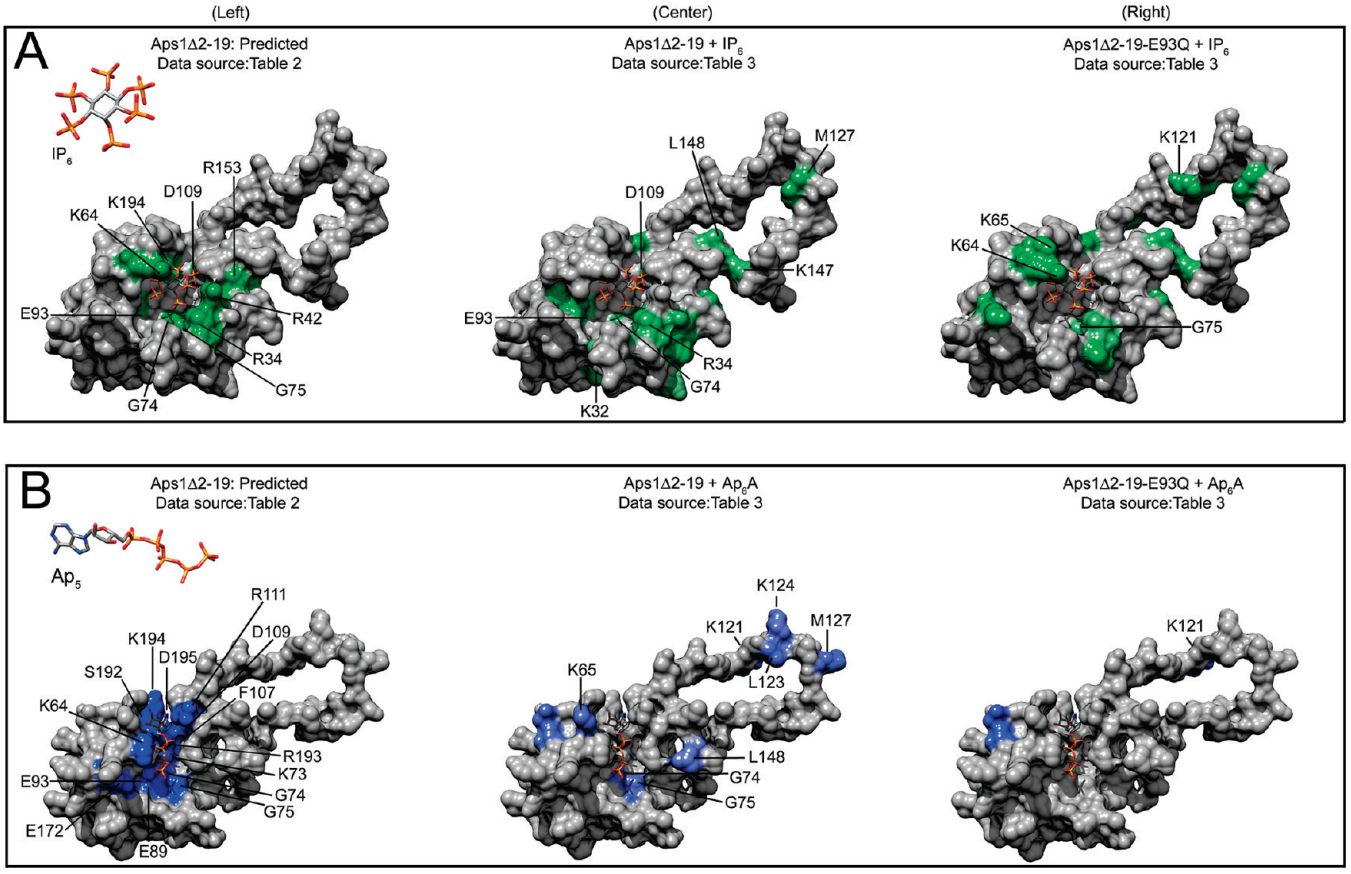

FIGURE 8: Residues involved in binding IP_6 and Ap_5 mapped on the structural models of Aps1Δ2−19. (A) Surface representation of a three-dimensional structural model of Aps1Δ2−19 generated by the HHpred homology modeling server (*19*) using the IP_6 ligand-bound human homologue DIPP1 (PDB ID: 2FVV) as the structural template. Structural models depict potential residues that bind the IP_6 ligand (left), residues exhibiting specific binding of IP_6 for Aps1Δ2−19 (center) and Aps1Δ2−19-E93Q (right). The residues are colored gray and with a gradient coloring scheme from gray to green that reflects the increasing magnitude of the chemical shift perturbation for each residue in the absence and presence of saturating amounts of ligand, respectively. (B) Surface representation of a three-dimensional structural model of Aps1Δ2−19 generated by the HHpred homology modeling server (*19*) using the Ap_5 ligand-bound Ndx1 (PDB ID: 1VC8) as the structural template. Structural models depict potential residues that bind the Ap_5 ligand (left), residues exhibiting specific binding of Ap_6A for Aps1Δ2−19 (center), and Aps1Δ2−19-E93Q (right). The residues are colored gray and with a gradient coloring scheme from gray to blue that reflects the increasing magnitude of the chemical shift perturbation for each residue in the absence and presence of saturating amounts of ligand, respectively. Residues most consistent with those anticipated to bind the respective ligands are marked. The data sources for the colored residues are indicated in the figure. The structural models were rendered using Chimera (*68*).

Conceivably, Y122 of Aps1Δ2−19, which is located in the dynamic loop (L6), can be positioned such that it participates in ring stacking to complement F107. However, no data were available for F107 and Y122 in Aps1Δ2−19 since they were not assigned. Nevertheless, site-directed mutagenesis studies of F84 in DIPP1, which is conserved as F107 in Aps1Δ2−19, indicate its importance with regard to Ap_6A hydrolysis, suggesting a role in substrate binding (*14*).

Clearly, further mutational and functional analyses are required to identify the role of each individual residue and the potential function of the large loop. If a mutated form of Aps1 can be generated such that it is specific for only one substrate, it would be of interest to conduct *in vivo* overexpression studies to confirm our previous hypothesis that Aps1 functions *in vivo* to degrade diphosphoinositol polyphosphates.

Finally, we hypothesize that Ndx1 is able to hydrolyze diphosphoinositol polyphosphates in addition to Ap_6A for two reasons. First, on a kinetic basis, *S. pombe* Aps1, *S. cerevisiae* Ddp1, proteins from the *H. sapiens* DIPP family, and murine DIPP3, which catalyze the hydrolysis of Ap_6A, also catalyze the hydrolysis of diphosphoinositol polyphosphates (*4*, *15*, *64*). In contrast, the nudix hydrolases *B. bacilliformis* IalA and human Ap_4A hydrolase, which exhibit a marked preference for Ap_4A as a substrate, exhibit negligible hydrolysis of diphosphoinositol polyphosphates (*4*). Second, on a structural basis, the volume and flexibility of the substrate binding site for enzymes that hydrolyze Ap_6A is probably large enough to accommodate a diphosphoinositol polyphosphate substrate. This is clearly true for human DIPP1 on the basis of its known structure and dual-substrate specificity (PDB ID: 2FVV) (*4*). The idea of a voluminous and flexible binding site was previously discussed by Cartwright and Mclennan (*65*) and is supported by the fact that Ap_6A can be hydrolyzed at different phosphate positions, resulting in a possibility of different pairs of products such as p_4A + ADP, p_5A + AMP, and ATP + ATP (*4*, *12*, *65*). In contrast, on the basis of the known structure of human Ap_4A hydrolase (*62*), it is highly probable that its binding site is too small to accommodate a diphosphoinositol polyphosphate, which is supported by the kinetic data cited above. In light of these observations, we hypothesize that, in general, enzymes that catalyze the hydrolysis of Ap_6A can also catalyze the hydrolysis of diphosphoinositol polyphosphates, while enzymes that catalyze the hydrolysis of Ap_3A or Ap_4A have little or no activity toward the diphosphoinositol polyphosphates.

ACKNOWLEDGMENT

We thank Drs. John Hart, Preston N. Garrison, Jens Wöhnert, Karyl I. Minard, and Patrick A. Joe for their thoughtful discussions as well as Angela K. Robinson and Jesse Ybarra for their technical expertise. We also thank Dr. Alex Taylor for providing the pET15b10H plasmid and Dr. John C. Lee for his gracious support.

SUPPORTING INFORMATION AVAILABLE

Table of the initial 10 top-ranking structural templates generated by HHpred for Aps1Δ2−19. This material is available free of charge via the Internet at http://pubs.acs.org.

REFERENCES

(1) Bateman, A., Coin, L., Durbin, R., Finn, R. D., Hollich, V., Griffiths-Jones, S., Khanna, A., Marshall, M., Moxon, S., Sonnhammer, E. L., Studholme, D. J., Yeats, C., and Eddy, S. R. (2004) The Pfam protein families database. *Nucleic Acids Res. 32*, D138–D141.

(2) Bessman, M. J., Frick, D. N., and O'Handley, S. F. (1996) The MutT proteins or "Nudix" hydrolases, a family of versatile, widely distributed, "housecleaning" enzymes. *J. Biol. Chem. 271*, 25059–25062.

(3) McLennan, A. G. (2006) The Nudix hydrolase superfamily. *Cell. Mol. Life Sci. 63*, 123–143.

(4) Safrany, S. T., Ingram, S. W., Cartwright, J. L., Falck, J. R., McLennan, A. G., Barnes, L. D., and Shears, S. B. (1999) The diadenosine hexaphosphate hydrolases from *Schizosaccharomyces pombe* and *Saccharomyces cerevisiae* are homologues of the human diphosphoinositol polyphosphate phosphohydrolase. Overlapping substrate specificities in a MutT-type protein. *J. Biol. Chem. 274*, 21735–21740.

(5) Dunckley, T., and Parker, R. (1999) The DCP2 protein is required for mRNA decapping in *Saccharomyces cerevisiae* and contains a functional MutT motif. *EMBO J. 18*, 5411–5422.

(6) van Dijk, E., Cougot, N., Meyer, S., Babajko, S., Wahle, E., and Seraphin, B. (2002) Human Dcp2: a catalytically active mRNA decapping enzyme located in specific cytoplasmic structures. *EMBO J. 21*, 6915–6924.

(7) Deana, A., Celesnik, H., and Belasco, J. G. (2008) The bacterial enzyme RppH triggers messenger RNA degradation by 5′ pyrophosphate removal. *Nature 451*, 355–358.

(8) Kloosterman, H., Vrijbloed, J. W., and Dijkhuizen, L. (2002) Molecular, biochemical, and functional characterization of a Nudix hydrolase protein that stimulates the activity of a nicotinoprotein alcohol dehydrogenase. *J. Biol. Chem. 277*, 34785–34792.

(9) Perraud, A. L., Fleig, A., Dunn, C. A., Bagley, L. A., Launay, P., Schmitz, C., Stokes, A. J., Zhu, Q., Bessman, M. J., Penner, R., Kinet, J. P., and Scharenberg, A. M. (2001) ADP-ribose gating of the calcium-permeable LTRPC2 channel revealed by Nudix motif homology. *Nature 411*, 595–599.

(10) Safrany, S. T., Caffrey, J. J., Yang, X., Bembenek, M. E., Moyer, M. B., Burkhart, W. A., and Shears, S. B. (1998) A novel context for the 'MutT' module, a guardian of cell integrity, in a diphosphoinositol polyphosphate phosphohydrolase. *EMBO J. 17*, 6599–6607.

(11) Gabelli, S. B., Bianchet, M. A., Xu, W., Dunn, C. A., Niu, Z. D., Amzel, L. M., and Bessman, M. J. (2007) Structure and function of the *E. coli* dihydroneopterin triphosphate pyrophosphatase: a Nudix enzyme involved in folate biosynthesis. *Structure 15*, 1014–1022.

(12) Ingram, S. W., Stratemann, S. A., and Barnes, L. D. (1999) *Schizosaccharomyces pombe* Aps1, a diadenosine 5′,5‴-P^1,P^6-hexaphosphate hydrolase that is a member of the nudix (MutT) family of hydrolases: cloning of the gene and characterization of the purified enzyme. *Biochemistry 38*, 3649–3655.

(13) Ingram, S. W., Safrany, S. T., and Barnes, L. D. (2003) Disruption and overexpression of the *Schizosaccharomyces pombe aps1* gene, and effects on growth rate, morphology and intracellular diadenosine 5′,5‴-P^1,P^5-pentaphosphate and diphosphoinositol polyphosphate concentrations. *Biochem. J. 369*, 519–528.

(14) Yang, X., Safrany, S. T., and Shears, S. B. (1999) Site-directed mutagenesis of diphosphoinositol polyphosphate phosphohydrolase, a dual specificity NUDT enzyme that attacks diadenosine polyphosphates and diphosphoinositol polyphosphates. *J. Biol. Chem. 274*, 35434–35440.

(15) Hua, L. V., Hidaka, K., Pesesse, X., Barnes, L. D., and Shears, S. B. (2003) Paralogous murine *Nudt10* and *Nudt11* genes have differential expression patterns but encode identical proteins that are physiologically competent diphosphoinositol polyphosphate phosphohydrolases. *Biochem. J. 373*, 81–89.

(16) Mildvan, A. S., Xia, Z., Azurmendi, H. F., Saraswat, V., Legler, P. M., Massiah, M. A., Gabelli, S. B., Bianchet, M. A., Kang, L. W., and Amzel, L. M. (2005) Structures and mechanisms of Nudix hydrolases. *Arch. Biochem. Biophys. 433*, 129–143.

(17) Dunn, C. A., O'Handley, S. F., Frick, D. N., and Bessman, M. J. (1999) Studies on the ADP-ribose pyrophosphatase subfamily of the nudix hydrolases and tentative identification of *trgB*, a gene associated with tellurite resistance. *J. Biol. Chem. 274*, 32318–32324.

(18) Xu, W., Dunn, C. A., Jones, C. R., D'Souza, G., and Bessman, M. J. (2004) The 26 Nudix hydrolases of *Bacillus cereus*, a close relative of *Bacillus anthracis*. *J. Biol. Chem. 279*, 24861–24865.

(19) Soding, J., Biegert, A., and Lupas, A. N. (2005) The HHpred interactive server for protein homology detection and structure prediction. *Nucleic Acids Res. 33*, 244–248.

(20) Ng, K. E., and Orgel, L. E. (1987) The action of a water-soluble carbodiimide on adenosine-5′-polyphosphates. *Nucleic Acids Res. 15*, 3573–3580.

(21) Robinson, A. K., de la Pena, C. E., and Barnes, L. D. (1993) Isolation and characterization of diadenosine tetraphosphate (Ap_4A) hydrolase from *Schizosaccharomyces pombe*. *Biochim. Biophys. Acta 1161*, 139–148.

(22) Ghosh, S., and Lowenstein, J. M. (1996) A multifunctional vector system for heterologous expression of proteins in *Escherichia coli*. Expression of native and hexahistidyl fusion proteins, rapid purification of the fusion proteins, and removal of fusion peptide by Kex2 protease. *Gene 176*, 249–255.

(23) Laemmli, U. K. (1970) Cleavage of structural proteins during the assembly of the head of bacteriophage T4. *Nature 227*, 680–685.

(24) Studier, F. W. (1973) Analysis of bacteriophage T7 early RNAs and proteins on slab gels. *J. Mol. Biol. 79*, 237–248.

(25) Barnes, L. D., Robinson, A. K., Mumford, C. H., and Garrison, P. N. (1985) Assay of diadenosine tetraphosphate hydrolytic enzymes by boronate chromatography. *Anal. Biochem. 144*, 296–304.

(26) Origin. (2000) Origin 6.0 . OriginLab Corp., Northampton, MA.

(27) Lee, H. J., and Wilson, I. B. (1971) Enzymic parameters: measurement of V and K_m. *Biochim. Biophys. Acta 242*, 519–522.

(28) Marley, J., Lu, M., and Bracken, C. (2001) A method for efficient isotopic labeling of recombinant proteins. *J. Biomol. NMR 20*, 71–75.

(29) Davis, R. W., Botstein, D., Roth, J. R., and Cold Spring Harbor Laboratory. (1980) Advanced Bacterial Genetics: A Manual for Genetic Engineering , Cold Spring Harbor Laboratory, Cold Spring Harbor, NY.

(30) Mori, S., Abeygunawardana, C., Johnson, M. O., and van Zijl, P. C. (1995) Improved sensitivity of HSQC spectra of exchanging protons at short interscan delays using a new fast HSQC (FHSQC) detection scheme that avoids water saturation. *J. Magn. Reson. B 108*, 94–98.

(31) Delaglio, F., Grzesiek, S., Vuister, G. W., Zhu, G., Pfeifer, J., and Bax, A. (1995) NMRPipe: a multidimensional spectral processing system based on UNIX pipes. *J. Biomol. NMR 6*, 277–293.

(32) Johnson, B. A. (2004) Using NMRView to visualize and analyze the NMR spectra of macromolecules. *Methods Mol. Biol. 278*, 313–352.

(33) Salzmann, M., Pervushin, K., Wider, G., Senn, H., and Wuthrich, K. (1998) TROSY in triple-resonance experiments: new perspectives for sequential NMR assignment of large proteins. *Proc. Natl. Acad. Sci. U.S.A. 95*, 13585–13590.

(34) Grzesiek, S., Anglister, J., and Bax, A. (1993) Correlation of backbone amide and aliphatic side-chain resonances in C-13/N-15-enriched proteins by isotropic mixing of C-13 magnetization. *J. Magn. Reson. B 101*, 114–119.

(35) Eghbalnia, H. R., Wang, L., Bahrami, A., Assadi, A., and Markley, J. L. (2005) Protein energetic conformational analysis from NMR chemical shifts (PECAN) and its use in determining secondary structural elements. *J. Biomol. NMR 32*, 71–81.

(36) Kay, L. E., Nicholson, L. K., Delaglio, F., Bax, A., and Torchia, D. A. (1992) Pulse sequences for removal of the effects of cross-correlation between dipolar and chemical-shift anisotropy relaxation mechanism on the measurement of heteronuclear T_1 and T_2 values in proteins. *J. Magn. Reson. 97*, 359–375.

(37) Angulo, J., Hricovini, M., Gairi, M., Guerrini, M., de Paz, J. L., Ojeda, R., Martin-Lomas, M., and Nieto, P. M. (2005) Dynamic properties of biologically active synethetic heparin-like hexasaccharides. *Glycobiology 15*, 1008–1015.

(38) Press, W. H., Flannery, B. P., Teukolsky, S. A., and Vetterling, W. T. (1992) Numerical Recipes in C: The Art of Scientific Computing , Cambridge University Press, New York.
(39) Freedberg, D. I., Ishima, R., Jacob, J., Wang, Y. X., Kustanovich, I., Louis, J. M., and Torchia, D. A. (2002) Rapid structural fluctuations of the free HIV protease flaps in solution: relationship to crystal structures and comparison with predictions of dynamics calculations. *Protein Sci. 11*, 221–232.
(40) Alexandrescu, A. T., Jahnke, W., Wiltscheck, R., and Blommers, M. J. (1996) Accretion of structure in staphylococcal nuclease: an ^{15}N NMR relaxation study. *J. Mol. Biol. 260*, 570–587.
(41) Ginalski, K. (2006) Comparative modeling for protein structure prediction. *Curr. Opin. Struct. Biol. 16*, 172–177.
(42) Fischer, D. (2006) Servers for protein structure prediction. *Curr. Opin. Struct. Biol. 16*, 178–182.
(43) Petrey, D., and Honig, B. (2005) Protein structure prediction: inroads to biology. *Mol. Cell 20*, 811–819.
(44) Battey, J. N., Kopp, J., Bordoli, L., Read, R. J., Clarke, N. D., and Schwede, T. (2007) Automated server predictions in CASP7. *Proteins 69* (Suppl 8), 68–82.
(45) Soding, J. (2005) Protein homology detection by HMM-HMM comparison. *Bioinformatics 21*, 951–960.
(46) Fiser, A., and Sali, A. (2003) Modeller: generation and refinement of homology-based protein structure models. *Methods Enzymol. 374*, 461–491.
(47) Collaborative Computational Project-Number 4 (1994) The CCP4 suite: programs for protein crystallography. *Acta Crystallogr., Sect. D 50*, 760−763.
(48) Hajduk, P. J., Boyd, S., Nettesheim, D., Nienaber, V., Severin, J., Smith, R., Davidson, D., Rockway, T., and Fesik, S. W. (2000) Identification of novel inhibitors of urokinase via NMR-based screening. *J. Med. Chem. 43*, 3862–3866.
(49) Dehner, A., Furrer, J., Richter, K., Schuster, I., Buchner, J., and Kessler, H. (2003) NMR chemical shift perturbation study of the N-terminal domain of Hsp90 upon binding of ADP, AMP-PNP, geldanamycin, and radicicol. *ChemBioChem 4*, 870–877.
(50) Kingston, R. L., Hamel, D. J., Gay, L. S., Dahlquist, F. W., and Matthews, B. W. (2004) Structural basis for the attachment of a paramyxoviral polymerase to its template. *Proc. Natl. Acad. Sci. U. S.A. 101*, 8301–8306.
(51) Robinson, N. E., and Robinson, A. B. (2001) Prediction of protein deamidation rates from primary and three-dimensional structure. *Proc. Natl. Acad. Sci. U.S.A. 98*, 4367–4372.
(52) Ou, H. D., Lai, H. C., Serber, Z., and Dotsch, V. (2001) Efficient identification of amino acid types for fast protein backbone assignments. *J. Biomol. NMR 21*, 269–273.
(53) Jimenez, B., Moratal, J. M., Piccioli, M., and Donaire, A. (2004) Mobility Studies in Proteins by 15N Nuclear Magnetic Resonance: Rusticyanin As an Example, in Methods in Proteome and Protein Analysis: Principles and Practice (Kamp, R. M., Calvete, J. J., and Choli-Papadopoulou, T., Eds.) pp 15−34, Springer, Berlin.
(54) Iwai, T., Kuramitsu, S., and Masui, R. (2004) The Nudix hydrolase Ndx1 from *Thermus thermophilus* HB8 is a diadenosine hexaphosphate hydrolase with a novel activity. *J. Biol. Chem. 279*, 21732–21739.
(55) Laskowski, R. A., MacArthur, M. W., Moss, D. S., and Thornton, J. M. (1993) Procheck-a program to check the stereochemical qualtity of protein structures. *J. Appl. Crystallogr. 26*, 283–291.
(56) Maksel, D., Gooley, P. R., Swarbrick, J. D., Guranowski, A., Gange, C., Blackburn, G. M., and Gayler, K. R. (2001) Characterization of active-site residues in diadenosine tetraphosphate hydrolase from *Lupinus angustifolius*. *Biochem. J. 357*, 399–405.
(57) Lin, J., Abeygunawardana, C., Frick, D. N., Bessman, M. J., and Mildvan, A. S. (1996) The role of Glu 57 in the mechanism of the *Escherichia coli* MutT enzyme by mutagenesis and heteronuclear NMR. *Biochemistry 35*, 6715–6726.
(58) Swarbrick, J. D., Bashtannyk, T., Maksel, D., Zhang, X. R., Blackburn, G. M., Gayler, K. R., and Gooley, P. R. (2000) The three-dimensional structure of the Nudix enzyme diadenosine tetraphosphate hydrolase from *Lupinus angustifolius* L. *J. Mol. Biol. 302*, 1165–1177.
(59) Chothia, C., and Lesk, A. M. (1986) The relation between the divergence of sequence and structure in proteins. *EMBO J. 5*, 823–826.
(60) Kinch, L. N., and Grishin, N. V. (2002) Evolution of protein structures and functions. *Curr. Opin. Struct. Biol. 12*, 400–408.
(61) Bailey, S., Sedelnikova, S. E., Blackburn, G. M., Abdelghany, H. M., Baker, P. J., McLennan, A. G., and Rafferty, J. B. (2002) The crystal structure of diadenosine tetraphosphate hydrolase from *Caenorhabditis elegans* in free and binary complex forms. *Structure 10*, 589–600.
(62) Swarbrick, J. D., Buyya, S., Gunawardana, D., Gayler, K. R., McLennan, A. G., and Gooley, P. R. (2005) Structure and substrate-binding mechanism of human Ap_4A hydrolase. *J. Biol. Chem. 280*, 8471–8481.
(63) Zuiderweg, E. R. (2002) Mapping protein-protein interactions in solution by NMR spectroscopy. *Biochemistry 41*, 1–7.
(64) Caffrey, J. J., Safrany, S. T., Yang, X., and Shears, S. B. (2000) Discovery of molecular and catalytic diversity among human diphosphoinositol-polyphosphate phosphohydrolases. An expanding Nudt family. *J. Biol. Chem. 275*, 12730–12736.
(65) Cartwright, J. L., and McLennan, A. G. (1999) The *Saccharomyces cerevisiae* YOR163w gene encodes a diadenosine 5′, 5‴-P^I,P^6-hexaphosphate (Ap_6A) hydrolase member of the MutT motif (Nudix hydrolase) family. *J. Biol. Chem. 274*, 8604–8610.
(66) Thompson, J. D., Gibson, T. J., Plewniak, F., Jeanmougin, F., and Higgins, D. G. (1997) The CLUSTAL-X windows interface: flexible strategies for multiple sequence alignment aided by quality analysis tools. *Nucleic Acids Res. 25*, 4876–4882.
(67) Kabsch, W., and Sander, C. (1983) Dictionary of protein secondary structure: pattern recognition of hydrogen-bonded and geometrical features. *Biopolymers 22*, 2577–2637.
(68) Pettersen, E. F., Goddard, T. D., Huang, C. C., Couch, G. S., Greenblatt, D. M., Meng, E. C., and Ferrin, T. E. (2004) UCSF Chimera: a visualization system for exploratory research and analysis. *J. Comput. Chem. 25*, 1605–1612.